Artificial intelligence velocimetry and microaneurysm-on-a-chip for three-dimensional analysis of blood flow in physiology and disease

Shengze Cai[a,1], He Li[a,1], Fuyin Zheng[b,c,1], Fang Kong[c], Ming Dao[b,2], George Em Karniadakis[a,d,2], and Subra Suresh[e,2]

[a]Division of Applied Mathematics, Brown University, Providence, RI 02912; [b]Department of Materials Science and Engineering, Massachusetts Institute of Technology, Cambridge, MA 02139; [c]School of Biological Sciences, Nanyang Technological University, 639798 Singapore; [d]School of Engineering, Brown University, Providence, RI 02912; and [e]Nanyang Technological University, 639798 Singapore

Contributed by Subra Suresh, February 8, 2021 (sent for review January 21, 2021; reviewed by José-Alain Sahel and M. Taher A. Saif)

Understanding the mechanics of blood flow is necessary for developing insights into mechanisms of physiology and vascular diseases in microcirculation. Given the limitations of technologies available for assessing in vivo flow fields, in vitro methods based on traditional microfluidic platforms have been developed to mimic physiological conditions. However, existing methods lack the capability to provide accurate assessment of these flow fields, particularly in vessels with complex geometries. Conventional approaches to quantify flow fields rely either on analyzing only visual images or on enforcing underlying physics without considering visualization data, which could compromise accuracy of predictions. Here, we present artificial-intelligence velocimetry (AIV) to quantify velocity and stress fields of blood flow by integrating the imaging data with underlying physics using physics-informed neural networks. We demonstrate the capability of AIV by quantifying hemodynamics in microchannels designed to mimic saccular-shaped microaneurysms (microaneurysm-on-a-chip, or MAOAC), which signify common manifestations of diabetic retinopathy, a leading cause of vision loss from blood-vessel damage in the retina in diabetic patients. We show that AIV can, without any a priori knowledge of the inlet and outlet boundary conditions, infer the two-dimensional (2D) flow fields from a sequence of 2D images of blood flow in MAOAC, but also can infer three-dimensional (3D) flow fields using only 2D images, thanks to the encoded physics laws. AIV provides a unique paradigm that seamlessly integrates images, experimental data, and underlying physics using neural networks to automatically analyze experimental data and infer key hemodynamic indicators that assess vascular injury.

blood flow in microaneurysm | diabetic retinopathy | three-dimensional flow fields | deep learning | image analysis

Human blood, primarily comprising plasma, red blood cells (RBCs), white blood cells, and platelets, is a non-Newtonian fluid exhibiting shear-thinning behavior (1, 2). The effect of this non-Newtonian behavior becomes more pronounced in microcirculation (3). Understanding and quantifying the biorheology of blood is essential for gaining insights into the mechanisms that influence microcirculation in physiology and disease (4–6). The characteristics of hemodynamics also determine the vascular integrity and blood-cell transport in physiology, e.g., the margination of platelets (7, 8). Platelet margination refers to the phenomenon of formation of a cell-free layer near the vessel wall in blood flow, as RBCs accumulate in the center of the vessel. Compromised hemodynamics can result in pathologies such as endothelial-cell inflammation and dysfunction, undesired platelet activation, and the formation of clots within a blood vessel (9–11).

Scientific research over the past several decades has led to rapid advances in in vivo imaging techniques (12–14). Despite this progress, it is currently not feasible to observe in real time many in vivo biological processes in microcirculation, such as the rupture of a microaneurysm (MA) in the retinal microvasculature and the initiation and development of blood clots. To compensate for this void in our ability to track the origins and progression of disease states, in vitro experiments of blood flow within microfluidic channels have been developed to mimic in vivo circulation under both physiologically and pathologically relevant conditions (see reviews in refs. 15–17). Microfluidic devices and laboratory-on-a-chip platforms offer advantages in exploring the biophysical and biochemical characteristics of blood flow in microvessels. Benefits of these devices include the need for only small volumes of blood for analysis and precise control over temperature, concentrations of gas, and chemicals in the blood (18). Another distinct advantage of such microfluidic platforms is that they enable quantitative determination of various key parameters associated with hemodynamics, such as spatial distributions of velocity and stress fields, under well-controlled experimental conditions so that mechanistic insights could be extracted for transitions from healthy to pathological states.

Significance

Microfluidics is an important in vitro platform to gain insights into mechanics of blood flow and mechanisms of pathophysiology of human diseases. Extraction of 3D fields in microfluidics with dense cell suspensions remains a formidable challenge. We present artificial-intelligence velocimetry (AIV) as a general platform to determine 3D flow fields and a microaneurysm-on-a-chip to simulate blood flow in microaneurysms in patients with diabetic retinopathy. AIV is built on physics-informed neural networks that integrate seamlessly 2D images from microfluidic experiments or in vivo observations with physical laws to estimate full 3D velocity and stress fields. AIV could be integrated into imaging technologies to automatically infer key hemodynamic metrics from in vivo and in vitro biomedical images.

Author contributions: S.C., H.L., M.D., G.E.K., and S.S. designed research; S.C., H.L., F.Z., and F.K. performed research; S.C., H.L., F.Z., F.K., M.D., G.E.K., and S.S. analyzed data; S.C., H.L., F.Z., F.K., M.D., G.E.K., and S.S. wrote the paper; and M.D., G.E.K., and S.S. supervised research.

Reviewers: J.-A.S., University of Pittsburgh School of Medicine; and M.T.A.S., University of Illinois at Urbana-Champaign.

Competing interest statement: S.C., H.L., M.D., G.E.K., and S.S. have filed a patent application based on the research presented in this paper.

[1]S.C., H.L., and F.Z. contributed equally to this work.

[2]To whom correspondence may be addressed. Email: SSuresh@ntu.edu.sg, George_Karniadakis@brown.edu, or mingdao@mit.edu.

This article contains supporting information online at https://www.pnas.org/lookup/suppl/doi:10.1073/pnas.2100697118/-/DCSupplemental.

Published March 24, 2021.

A wide variety of experimental techniques are currently available to assess the hemodynamics of in vitro blood flow in microcirculation. The state-of-the-art optical whole-field velocity measurement technique is microparticle image velocimetry (μPIV) (19, 20), a nonintrusive method used to estimate flow fields in microchannels. Various algorithms employing μPIV have been well developed in recent years (21–23), and this technology has been successfully applied to a broad range of biological problems (see reviews in refs. 24–26). μPIV can provide measurements of blood velocity along channels in microcirculation, with high spatial and temporal resolution, by analyzing the motion of laser-induced fluorescence tracers seeded into blood (27–29). However, the experimental apparatus requires elaborate calibration and may not be amenable for wide or easy deployment. Other approaches to monitor flow motion, such as advanced PIV methods (30–32) or optical flow monitoring techniques (33–36), are able to quantify hemodynamics from images of blood flow in the microchannels using RBCs and platelets as tracers, thereby requiring less hardware. However, their accuracy in providing near-wall flow measurements, which is critical for inferring the pathogenic basis of blood rheology and the estimation of wall shear stress, could be compromised, owing to the formation of cell-free layers in the vicinity of blood vessel walls.

Computational fluid dynamics (CFD) models have also been employed to simulate blood flow in microvessels or channels to investigate the pathophysiology of circulatory diseases (37, 38). By invoking laws of physics (e.g., Navier–Stokes equations) and specific boundary conditions (such as no-slip conditions at the blood-vessel wall), CFD models can simulate the flow field and extract key hemodynamic indicators. Several studies have employed CFD models to compute flow and stress fields in normal microvessels, as well as channels with various shapes, such as stenotic channels [in which constricted flow from plaques markedly alters flow characteristics (39, 40)], aneurysmal vessels containing a bulge in the vessel as a result of a weakened vessel wall (41, 42), and other vasculatures with complex geometries (43, 44). However, results extracted from CFD models are very sensitive to the flow-boundary conditions assumed at the inlets and outlets, which can be patient-specific. Even moderate errors in flow-boundary conditions could lead to large uncertainty in the estimation of the flow fields (45). In addition, CFD simulations could be computationally cumbersome for modeling flow field with moving boundaries or geometric variation, such as the hemodynamics changes due to accumulation of blood cells.

Problem Description

Accurate assessment of hemodynamics in microvessels requires both experimental data extracted from controlled in vitro or in vivo assays and application of relevant laws of physics. In this work, we propose artificial-intelligence velocimetry (AIV), a unique computational framework that infers velocity fields and stress fields from two-dimensional (2D) images that are interpreted by using artificial-intelligence techniques based on underlying physical principles. In particular, AIV is developed based on the physics-informed neural networks (PINNs) (47, 48), which can automatically infer these flow fields in arbitrary domains by seamlessly integrating data from in vivo or in vitro with the governing equations of fluid flow. As illustrated in Fig. 1, with spatial coordinates and time, (x, y, z, t), as inputs, AIV uses a fully connected network to approximate the functional solutions of image intensity I, velocity field (u, v, w), and pressure field p. The loss function for training the neural network is composed of three terms: the mismatch between the network predictions and data ($\mathcal{L}_{data}$); residuals of the governing equations ($\mathcal{L}_{res}$); and boundary conditions ($\mathcal{L}_{bcs}$) on the channel surfaces. Here, we assume no-slip boundary conditions on the channel wall as cell-free layers are observed in the vicinity of the wall (see the bright-field images in Fig. 2 *B* and *C*). This observation is also consistent with the finding from studies of blood flow in a microchannel with similar dimensions (49). Slip boundary conditions can also be employed in AIV by modifying the formulations of $\mathcal{L}_{bcs}$ in the case of blood flow in the capillary (50), where the membrane of the moving blood cells are constantly in contact with the vessel wall or when the permeability of the vessel wall needs to be considered, e.g., blood flow through atherosclerotic plaques where deposition of cholesterol could increase the permeability of the arterial wall (51, 52). More details of the AIV model can be found in *Materials and Methods* and *SI Appendix*.

To demonstrate the capability of AIV based on a sequence of 2D microscopic blood-flow images, we first apply it to infer the velocity and stress fields in three-dimensional (3D) microchannels. As shown in Fig. 2 *A* and *B*, we design a microfluidic system, termed Micro-Aneurysm-On-A-Chip (MAOAC), to mimic MAs, which are the earliest clinically visible signs of diabetic retinopathy (DR), a complication of diabetes that could lead to visual impairment and blindness in diabetic patients (53). MAOAC contains eight straight microchannels intersecting with various sizes of cavities to mimic saccular-shaped MAs, the most prevalent shape of MAs observed in the retinal microvasculature of DR patients (54, 55). A high-speed camera is used to record blood flow in the microchannel (Fig. 2*C*). In addition, laser-induced fluorescence is employed to track the motion of platelets (Fig. 2*D*). More details of the experimental setup can be found in *Materials and Methods*. We adopt AIV to quantify key indicators of hemodynamics, such as velocity profiles, pressure, and wall shear stress, for various MAs and investigate alterations

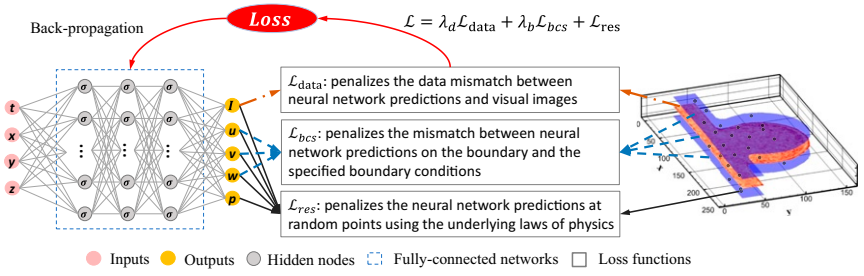

Fig. 1. Schematic diagram of AIV. A fully connected neural network is used to approximate solutions to desired output parameters, (I, u, v, w, p), by considering space and time coordinates as inputs (x, y, z, t). The governing equations are encoded in the network, where the derivatives are computed via automatic differentiation in the TensorFlow code [Google (46)]. No-slip boundary conditions on the channel surfaces (including upper, lower, and lateral walls) are also introduced, namely, $\mathbf{u}(\partial\Omega) = 0$. The activation function for each neuron is $\sigma(\cdot) = \sin(\cdot)$. The parameters of the neural network are trained by minimizing the loss function, which is composed of three terms: data mismatch, wall boundary conditions, and residuals of all conservation laws. More details of the proposed framework are described in *Materials and Methods* and *SI Appendix*.

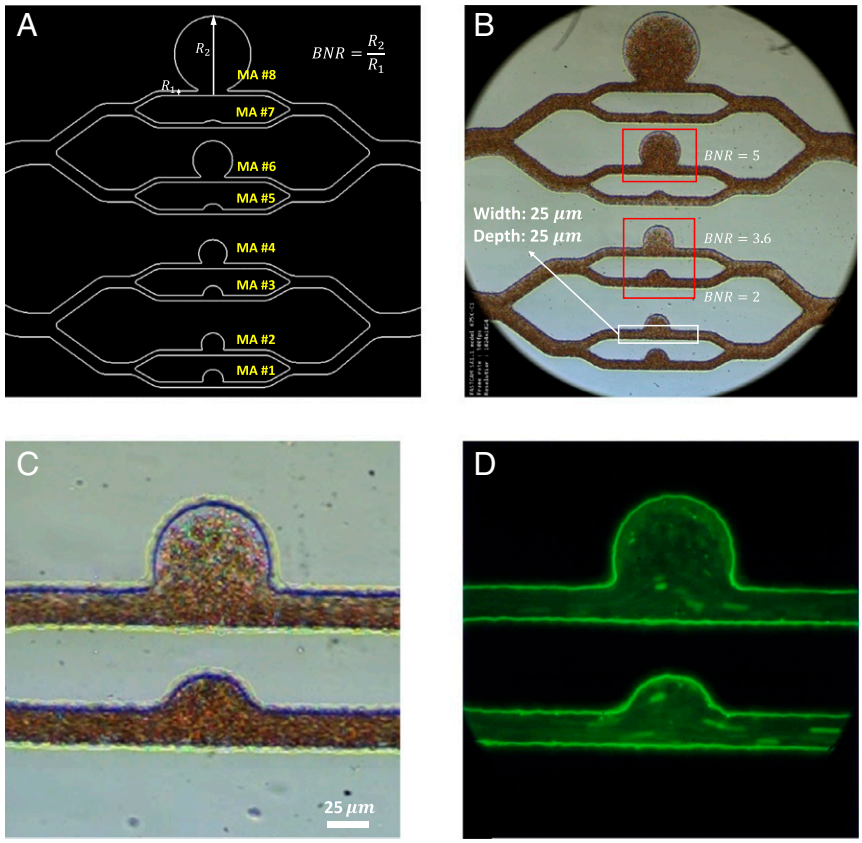

Fig. 2. Design and microscopic images of the microfluidic platform, MAOAC. (*A*) Schematic diagram of the MA PDMS channels with different sizes. The size of the MA is characterized by the BNR, which is defined as the largest dimension of the MA body (R_2) divided by the diameter of feeding vessel (R_1). The BNR of MA on MAOAC is varied from 1.5 to 12. The cross-section of the microchannel at the inlet and outlet portions is a square with an edge size of 25 μm. (*B*) An overview of a bright-field image illustrating blood flow in the microchip. (More details can be seen in Movie S1.) (*C*) A higher-magnification view of the bright-field image of two MA channels (BNR = 2 and BNR = 3.6). (*D*) A fluorescence-stained image of the same two MA channels shown in *C*. (More details can be seen in Movie S2.) AIV is used to extract velocity and pressure fields from the bright-field video images focusing on MAs with three typical sizes, namely, BNR = 2, 3.6, and 5, which are highlighted by the red rectangles in *B*. For MAs with BNR = 2 and 3.6, we perform platelet tracking on the fluorescence-stained video (*D*) for validation of AIV.

in hemodynamics induced by the change in size of MAs. In order to evaluate the performance of AIV, we compare the results from AIV with those obtained from five different experimental and computational methods: optical flow (36), Deep-PIV (56), single-cell tracking, CFD (57), and DPD (58).

Results

Inferring 2D Flow Fields. To demonstrate the capability of AIV to quantify the velocity and stress fields from microfluidic images during blood flow, we first extract 2D flow fields, such as velocity profile, pressure, and wall shear stress, from a sequence of 2D images taken in MAOAC and obtain the critical hemodynamic metrics. As shown in Fig. 2*B*, we select sequential images from three channels (MA#3, MA#4, and MA#6), representing a small MA (body-to-neck ratio [BNR] = 2), an intermediate MA (BNR = 3.6), and a large MA (BNR = 5). Since the depth of these microchannels is only 25 μm, we assume that the movement of RBCs captured by the microfluidic flow images occurs at the middle plane in the channel-depth direction such that the image data can be converted to a 2D spatiotemporal scalar field $I(x, y, t)$. Fig. 3 *A*–*C* show the 2D velocity fields, pressure fields, and shear stress profiles in the three MA channels based on the sequence of bright-field images in Fig. 2*B*. We observe that the maximum flow velocities in the inlet regions of the three MAOAC channels are about 1.5 mm/s, and the velocities drop along with pressure and shear stress when the flow enters the lumen of MAs. The decrease in velocity, pressure, and shear stress becomes more pronounced as the size of the MA increases. These alterations in hemodynamics are essential to gain a better understanding of the pathophysiology of MAs, since prior studies clearly suggest that reduced wall shear stress could cause endothelial dysfunction (59), which serves as a catalyst for the growth of aneurysms (60).

To further assess the reliability and accuracy of AIV, we compare our estimates with results obtained from three other independent approaches: the conventional optical flow method (36), Deep-PIV [an advanced PIV method with convolutional neural networks (32, 56)], and manual platelet tracking using the fluorescent images in our experiments. The implementation of the optical flow and Deep-PIV methods for predicting the fields in the present geometrical arrangements is described in *SI Appendix*. The velocity comparisons shown in Fig. 4 are performed at two points along vertical cross-lines of the microchannels: one located at the postaneurysm channel (Line #1, at $x = 50$ μm, as seen in Fig. 3) and the other one crossing the deepest region of the MA (Line #2, at $x = 130$ μm as seen in Fig. 3). The velocity profiles along Line #1 for the three microchannels (Fig. 4) show that our AIV model predictions of bulk flow velocities are consistent with the results from Deep-PIV and are less than 10% higher than the results from optical flow around the center of the channels. As for the near-wall velocity estimation, both Deep-PIV and optical flow techniques predict a

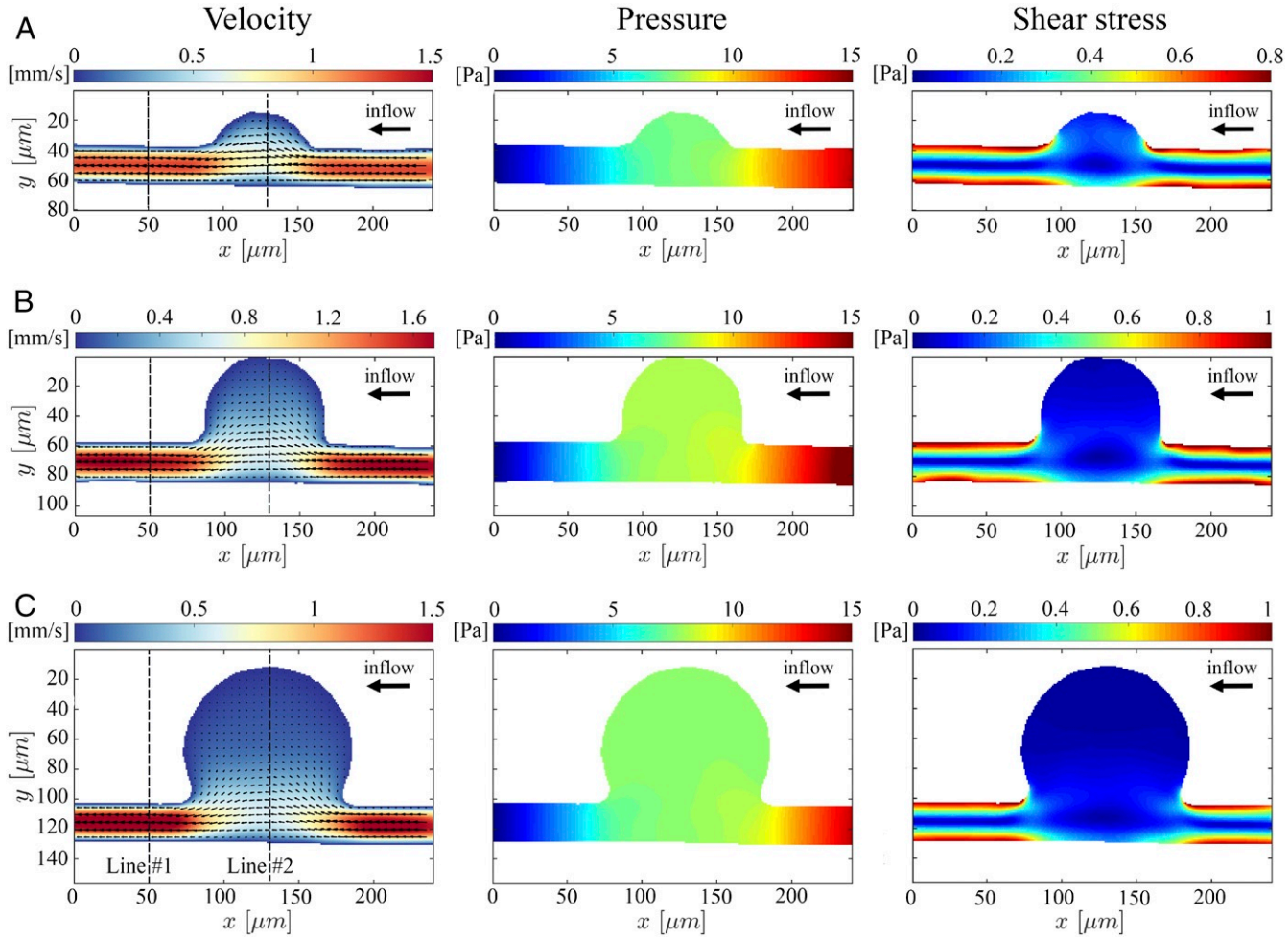

Fig. 3. The 2D AIV predictions of velocity, pressure, and shear stress fields in MAOAC channels for BNR = 2 (*A*), BNR = 3.6 (*B*), and BNR = 5 (*C*). In *Left*, the arrows indicate the direction of the flow, whereas the color represents the magnitude of the velocity. AIV results are averaged over 100 image frames. The spatial distribution of the fields is represented by the colors in all of the plots.

nonvanishing velocity on the channel wall, whereas the AIV model gives zero velocity on the wall due to the imposition of the no-slip boundary condition. For velocity profile along Line #2, the AIV model predictions of the bulk flow velocity are in good agreement with the results of Deep-PIV and optical flow for all three MAOAC channels, but only AIV achieves zero velocity for near-wall predictions, as a consequence of the imposed boundary condition.

In addition to the above comparisons, we also performed a cross-validation of AIV by manually tracking the motion of platelets from fluorescence-stained video. As shown in Fig. 5*A*, four trajectories are identified for tracking the motion of four different platelets or platelet aggregates, with platelet velocities calculated along each of these trajectories. We also extract flow velocities along the same trajectories from velocity fields estimated by AIV in Fig. 5*B* for further comparison. To rationalize our approximation of local flow velocities using platelet velocities, we performed dissipative particle dynamics (DPD) simulations to model the transport of RBCs and platelets in channel MA#4 (BNR = 3.6), as shown in Fig. 6*A*. (Details of DPD simulation can be found in *SI Appendix*.) The trajectories of RBCs and platelets in Fig. 6*B* illustrate that in the straight channel, RBCs mostly travel in the core, where the flow velocity is high. This validates the assumptions, discussed earlier, that underlie our AIV framework. The platelets, however, flow in the cell-free layer near the vessel wall where the blood flow velocity is low, consistent with experimental and analytical studies (61–64). As a result, the displacement of platelets in the straight channel (Fig. 6*C*) is much smaller than that of RBCs during the same time interval. On the other hand, Fig. 6 *B* and *C* also show that the trajectories of RBCs and platelets overlap in the MA and that their displacements are comparable during the same time interval. These observations suggest that the velocities of platelets can be used to approximate local blood-flow velocities when platelets move within MAs.

Velocity estimates along the four trajectories are plotted in Fig. 5*C*. These results show that the AIV predictions are in good agreement with velocities calculated from the two trajectories (Traj-3 and Traj-4) of platelets traveling in the MAs in channel MA#4. This demonstrates the capability of AIV to accurately infer flow fields in blood microcirculation. At platelet trajectories further away from the perimeter of the MA, such as those along Traj-1 and Traj-2, the differences between AIV (on RBC trajectories) and platelet tracking become more accentuated, as anticipated from the effect of platelet margination.

Extracting 3D Flow Field from 2D Images. Next, we demonstrate that AIV can infer the full 3D flow velocity profiles along the entire depth of the microchannel using 2D images by invoking

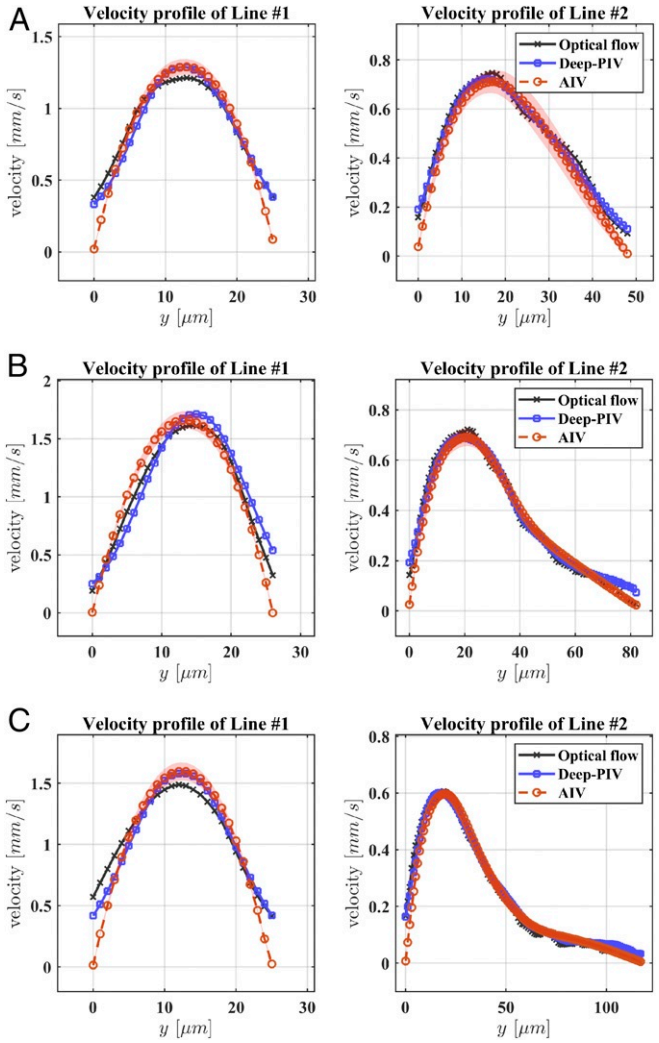

Fig. 4. Comparison of the velocity profiles predicted by AIV, conventional optical flow, and Deep-PIV along two cross-lines in MAOAC channels with BNR = 2 (*A*), BNR = 3.6 (*B*), BNR = 5 (*C*). Comparisons are performed along two dotted lines marked at Fig. 3, *Left*. Line #1 is selected at the outlet portion of the microchannel, whereas Line #2 crosses the deepest region of the MAs. The symbols representing AIV predictions signify time-averaged values from 100 image frames, and the shadows represent SDs.

the underlying physical laws of fluid flow. Such estimation cannot be accomplished by using existing methods, such as Deep-PIV or optical flow, due to the lack of data at different depths of the channel. In order to obtain 3D velocity profiles, as shown in Fig. 7*A*, we extend our computational domain along the depth direction (z) by 25 μm ($z \in [-12.5, 12.5]$ μm), in line with the depth of the MAOAC channels. We enforce the no-slip boundary condition on the upper and lower surfaces ($z = \pm 12.5$ μm) and the lateral channel walls such that $(u, v, w)_{\partial\Omega} = 0$. Similar to the 2D case, we assume that the movement of RBCs occurs primarily at the middle plane along the channel depth, so that data from the images can be converted to a 3D spatiotemporal scalar field $I(x, y, z = 0, t)$. A schematic of the AIV model, which is based on 3D physics-informed neural networks, is illustrated in Fig. 1 and in *SI Appendix*. Note that while the image data correspond to a 2D plane, the points for computing the residual loss $\mathcal{L}_{res}$ are uniformly selected in the 3D domain. The training process for the 3D cases is similar to that for 2D, which can be found in *SI Appendix*.

Fig. 7 *B* and *C* illustrate the velocity and pressure fields inferred by the AIV model at three different depth positions of the MA#6 channel (BNR = 5): $z = 0$ (middle plane) and $z = \pm 7.5$ μm. These results show that the flow velocities measured at $z = \pm 7.5$ are significantly smaller than those at the middle plane, whereas no notable changes are observed in the flow pressure here in the depth direction. The shear stress on the channel wall is illustrated in Fig. 7*D*, and it shows a sudden drop of the wall shear stress from the parent vessel to the vessel wall of the MA. The wall shear stress continues to decrease in the region further away from the feeding channel, consistent with our 2D predictions and the findings reported from prior studies (42, 59, 65).

To evaluate the 3D results from AIV, we perform a companion 3D CFD simulation using the same governing equations (Eq. **2** in *Materials and Methods*) and computational domain as in the AIV method. We also employ the Carreau–Yasuda rheology model (Eq. **3**) to capture the shear-thinning behavior of the blood. The governing equations are solved by using *Nektar*, a fast CFD solver based on the spectral element method (57). We use the pressure difference between the channel inlet and the outlet from the AIV model to drive blood flow in the channel. As shown in Fig. 8*A*, the velocity fields inferred from the 3D AIV and those obtained from the CFD simulations for MA#6 are compared at two cross-sections of the microchannels, with one located at the postaneurysm channel and the other one

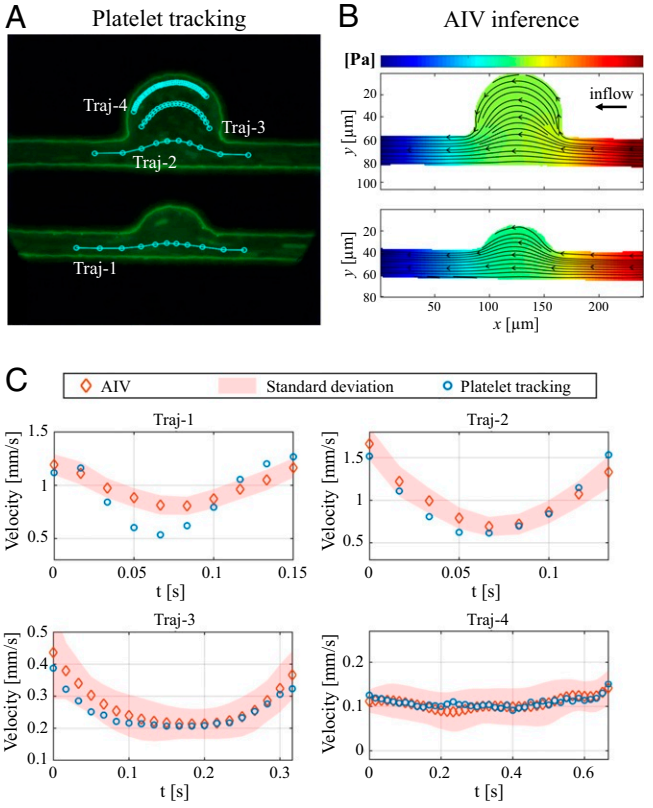

Fig. 5. Comparison of the velocities predicted by AIV and platelet tracking along four platelet trajectories in two MAOAC channels with BNR = 2 and 3.6. (*A*) Four platelet trajectories are tracked by using video images capturing experiments with fluorescence-staining. The velocity is computed as $V = |\mathbf{x}^{k+1} - \mathbf{x}^{k}|/\delta t$, where $\mathbf{x}^{k}$ and $\mathbf{x}^{k+1}$ are the positions of a platelet at two consecutive time steps with $\delta t = 1/60$ s. (*B*) The velocity magnitudes along these four trajectories are also extracted with AIV using bright-field video. (*C*) Magnitudes of velocity calculated along four trajectories using AIV and platelet tracking. The symbols representing AIV predictions signify the time-averaged values from 100 image frames, and the shadows represent the SDs.

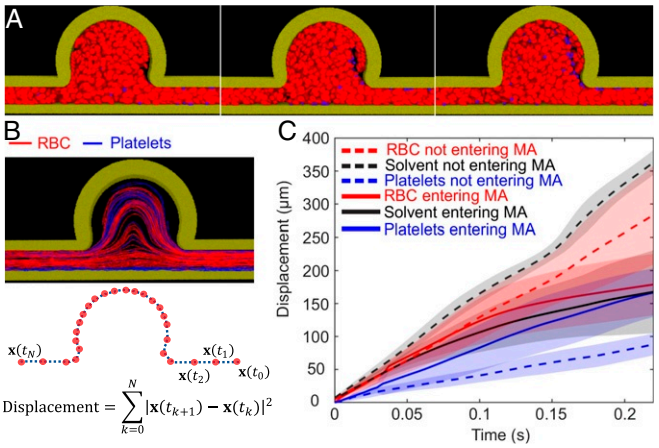

Fig. 6. Simulation of RBC and platelet transport in MAOAC channel with BNR = 3.6. (*A*) Three sequential snapshots (from left to right) of RBCs and platelets traveling in the microchannel. Red, RBCs; blue, platelets. Solvent particles are not plotted here to preserve clarity of presentation. (*B*) Trajectories of RBCs and platelets in the microchannel, as well as calculation of the displacements of RBCs and platelets based on their trajectories. Red curves, RBCs; blue curves, platelets. (*C*) Displacements of RBCs, platelets, and solvent particles as functions of time. The dotted lines signify displacements of RBCs, platelets, and solvent particles that do not travel into the MAs, whereas the solid lines designate the displacements of RBCs, platelets, and solvent particles that travel into the MAs. Each curve represents the average of 15 samples randomly selected from the simulation, except that the solvent particles which do not travel into the MAs were selected randomly around the centerline of the postaneurysm channel.

crossing the deepest region of MAs. The velocity maps of these two cross-sections in Fig. 8 *B* and *C* show that the predictions of AIV agree with the results of the CFD simulations. The maximum relative L_2-norm errors for these two cross-sections are calculated to be 8.9% and 9.6%, respectively. We further plot the velocity profiles at these two cross-sections along the lines of $z = 0$ μm and $z = 5.5$ μm (Fig. 8 *D* and *E*). These results also show good agreement between the AIV model and 3D CFD simulation. In particular, Fig. 8 *D* and *E* demonstrate that 3D AIV can capture the expected decay of the velocity along the z-direction. There are some differences between the predictions of the AIV model and the CFD model, although both models invoke the same physical laws (Eq. **2**), constitutive equation (Eq. **3**), and boundary conditions. We also plot the AIV-prediction and the CFD-simulation results of shear stress along two lines on two different planes in the channel-depth direction ($Z = 0$ μm and $Z = 3.5$ μm), which can be found in *SI Appendix*, Fig. S3. Our results show that AIV predictions are comparable with the CFD simulation results with an averaged error of $\sim 10\%$. These differences are attributed to the fact that AIV directly incorporates the flow-image data of RBCs in estimating the fields and thus provides a more realistic picture of blood flow in the microchannel than CFD models. Similar trends are also observed for the 3D velocity estimates for the MA#3 channel, which can be found in *SI Appendix*.

Discussion and Concluding Remarks

In this work, we have developed a unique model to determine the 3D velocity, pressure, and stress fields associated with human blood flow in microcirculation by synergistically integrating the underlying physics with sequential images from microfluidics experiment and machine learning. The advantage of the proposed AIV model is that the conservation laws of the physics of blood flow and no-slip boundary conditions are encoded into a deep-learning neural network to interpret direct experimental observations from a microfluidics platform. We note that the flow velocity boundary conditions (slip or nonslip) on the channel wall in AIV can be specified by the user, depending on the particular case of interest. Therefore, the predictions of near-wall velocity by AIV are more physiologically relevant than those measured from optical flow and μPIV. This feature is crucial for evaluating the wall shear stress, a hemodynamic metric that is associated with many vascular diseases (4, 6, 59). In distinct

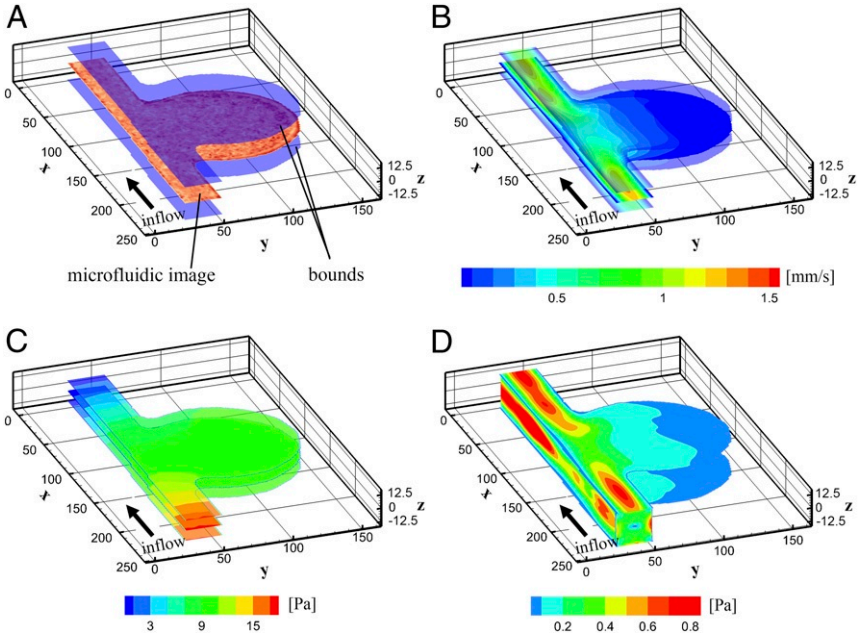

Fig. 7. The 3D AIV predictions for MAOAC channel with BNR = 5. (*A*) A 3D computational domain is constructed by extending the 2D domain along the depth direction (*z*) by 25 μm ($z \in [-12.5, 12.5]$ μm), consistent with the depth of the MAOAC channels. The images capture the motion of RBCs at the middle plane of the channel depth direction ($z = 0$). (*B* and *C*) Velocity (*B*) and pressure fields (*C*) at three different cross-sections ($z = 0, \pm 7.5$ μm) along the depth of the channel. (*D*) Shear stress on the channel wall. AIV results are averaged over 100 image frames.

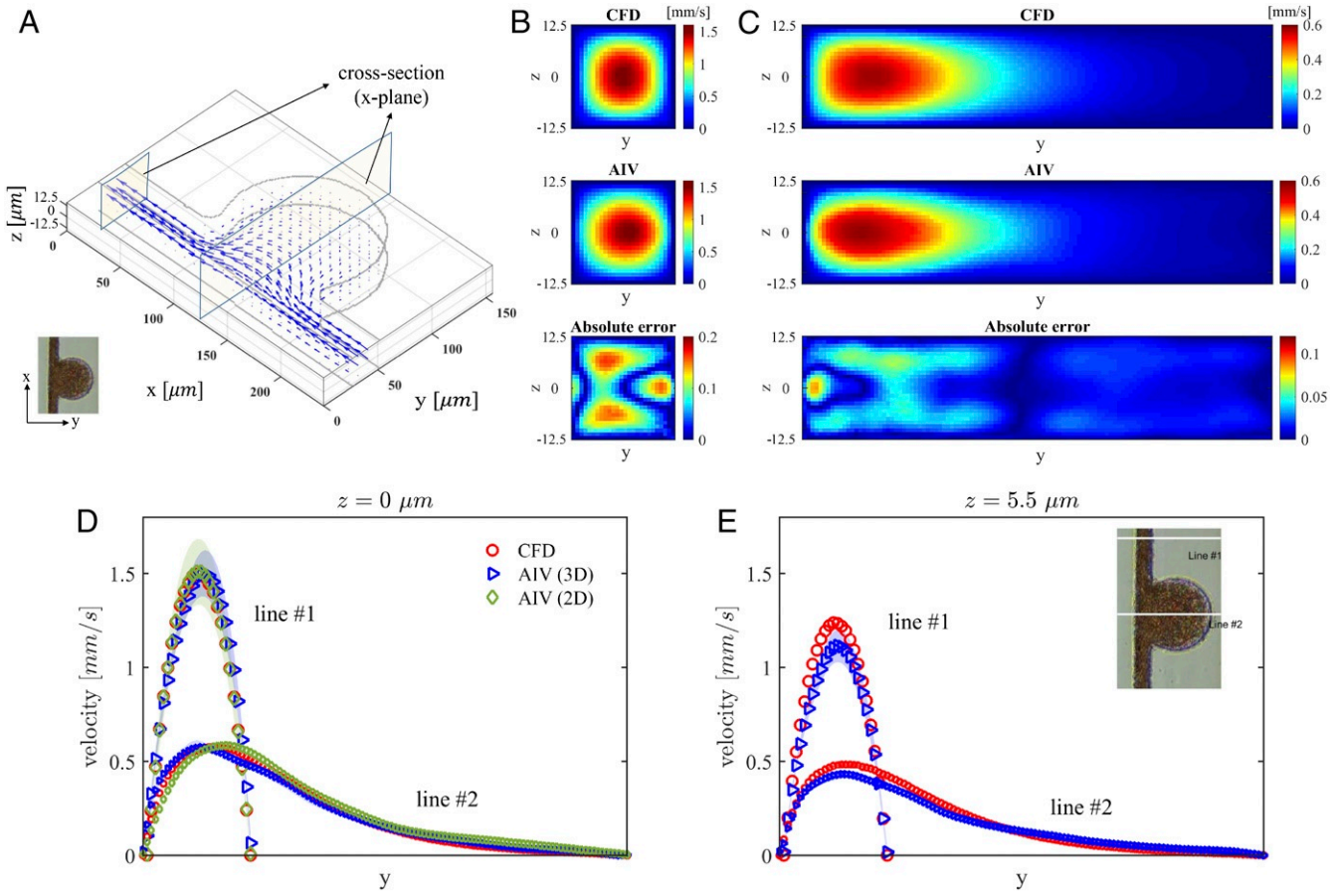

Fig. 8. Comparison of 3D AIV predictions with results of CFD simulations for the MAOAC channel with BNR = 5. (*A*) The 3D velocity vectors inferred from AIV. Two cross-sections along the x axis are selected for comparison with CFD simulations. (*B*) Velocity at the cross-section located at $x = 15$ μm in the microchannel. From top to bottom: CFD simulation, AIV model, and absolute error. The relative L_2-norm error at this cross-plane is 8.9%. (*C*) Velocity magnitudes at the cross-section located at $x = 130$ μm in the microchannel. From top to bottom: CFD simulation, AIV model, and absolute error. The relative L_2-norm error is 9.6%. (*D* and *E*) Velocity profiles along two cross-lines at planes $z = 0$ μm and $z = 5.5$ μm. The symbols representing AIV predictions signify the time-averaged values from 100 image frames, and the shadows represent the SDs.

contrast to CFD methods, whose results are very sensitive to flow boundary conditions at the inlets and outlets, AIV does not require a priori knowledge of these boundary conditions to estimate flow fields. This unique feature overcomes the challenge in many applications, where the exact pressure profiles at the local inlet(s) and outlet(s) of an in vitro microfluidic device or a capillary bed in vivo are difficult or even impossible to measure directly or approximate. Moreover, the AIV model is more effective than CFD simulation when making a prediction of the flow field undergoing dynamic changes due to moving boundaries, such as the prediction of blood flow within deformable vessel wall or changes of hemodynamics in the MA due to blood clotting, as observed from high-resolution adaptive optics scanning laser ophthalmoscopy (AOSLO) images (42) and histology studies (66).

To validate the present approach, we compare the predictions of AIV models on the full spectrum of key hemodynamic parameters, such as pressure differential, shear rate, and wall shear stress, with results obtained from five different experimental and computational methods: optical flow (36), Deep-PIV (56), single cell tracking, CFD simulations (57), and DPD (58). Our results show that AIV predictions of bulk flow velocities in MAOAC with different geometries are in agreement with results from these other independent methods. In contrast to CFD models, AIV is capable of inferring flow field on-the-fly in microchannels because of its flexibility to incorporate data from sequential experimental images, particularly with fluids, such as blood, with a heterogeneous composition. On the other hand, we demonstrate that AIV can infer, owing to the encoded physics laws, full 3D flow fields along the depth of the microchannel from a sequence of 2D images. This is difficult to achieve with conventional μPIV or other methods to estimate particle movement, which require advanced experimental apparatus, such as stereoscopic or holographic PIV (67, 68), to generate image data at different depths of the channel.

The present experimental results also provide insights and quantitative details to rationalize a variety of clinical findings pertaining to MAs in DR. The predictions of the flow field using MAOAC and AIV show reduced flow velocity and wall shear stress in the MAs with different BNR. Particularly, as the BNR of the MAs increases, the decrease in shear stress near the channel wall of the MAs becomes more significant. These results provide a rationale for the clinical finding that endothelial dysfunction, which is manifested as increased von Willebrand factor expression on the endothelial cell, is more likely to occur in MAs with larger BNR due to the reduced wall shear stress (59). We note that AIV can assess the blood-flow velocity for different shapes of MAs, such as focal bulging, fusiform, mixed saccular/fusiform, and so on. In this paper, we designed the microchannels to mimic various sizes of saccular-shaped MAs, because they are the most prevalent shape of MAs observed in the retinal microvasculature of DR patients. Future studies could employ

additional microfluidic geometry designs to address different types of MAs.

The altered hemodynamics in MAs also contributes to thrombosis in the vascular lumen of MAs, a recently documented pathology of DR (42). In vivo images obtained from AOSLO have been used to classify the MAs' morphologies into different groups (54), as well as to detect the blood clotting inside MAs (42). The AIV model can potentially be used to interpret the AOSLO images and predict the thrombus formation or rupture of MAs by monitoring the key hemodynamic metrics, such as wall shear stress, which is associated with the inflammation and dysfunction of endothelium cell, as well as the shear rate and the platelet residence time in the MAs, which can be used to predict the platelet activation and aggregation. We note that quantification of hemodynamic parameters from in vivo measurements in previous studies (42, 59, 65) were performed by using CFD models with assumed and general inflow and outflow boundary conditions since patient-specific inflow velocity was not readily available from in vivo images. The present AIV model, which does not require implementation of flow boundary conditions and mesh generation, can potentially learn the flow fields directly from in vivo video images and provide more accurate evaluation of hemodynamic indicators.

The AIV model proposed in this work can also be extended to accommodate various data sources through a multifidelity (MF) framework (69, 70), where additional neural networks are used to learn the correlation between the low-fidelity (e.g., simulation) and high-fidelity (e.g., experimental) data. The MF framework is very effective when there is a dearth of reliable, high-fidelity data and, thus, could be particularly useful for learning from in vivo images whose resolution and quality may be limited. For example, when only a portion of the flow field can be observed from in vivo images or only measurements of the velocity along a limited set of trajectories are available (e.g., by tracking local displacements of blood cells), we could first perform 3D CFD simulations to evaluate the flow field. These simulation data are considered low-fidelity data, as they are sensitive to the inflow and outflow boundary conditions, which are not always available from in vivo measurements. Following this, the 3D simulation data (low fidelity) could be integrated with the partial velocity field estimated by AIV based on in vivo images (high fidelity) using the MF framework to predict the entire flow field.

Although we have demonstrated several advantages of AIV over conventional methods, we also note some limitations of the AIV model. First, the computational cost of training the AIV model could be higher than the cost of optical flow or μPIV methods because of the need to solve the governing equations of the underlying physics laws. Application of multigraphics-processing unit training could help boost computational efficiency. Moreover, the trained AIV model could be used as a pretrained network to initialize the training of a new AIV model for other microfluidic experiments, thereby reducing the computational cost for future tasks. In this work, we assume that the flow of RBCs captured by sequential 2D images occurs at the middle plane in the channel-depth direction ($z = 0$). However, the 2D measurement plane generally has a certain finite thickness, which is determined by the depth of field of the objective lens. Incorporating the movement of RBCs out of the middle plane could lead to an underestimation of cross-sectional velocities. To extend the application of AIV to assess in vivo blood flow, we may need to consider the flow pulsatility as well as the dynamic deformation of the blood vessel wall. While AIV can naturally learn the pulsatile flow from image data, the underlying physics laws encoded in the AIV model need to be revised to account for the effect of deformable flow boundaries. For example, we can encode fluid-governing equations formulated on the basis of the arbitrary Lagrangian–Eulerian method, which is a standard approach to solve dynamic problems involving fluid–structure interaction and deformation of flow boundary (71, 72).

In summary, we present AIV, a unique platform that is capable of automatically inferring blood-flow field in microfluidic channels, and compute key hemodynamic parameters that are associated with the pathophysiology of MAs, one of the earliest clinically visible signs of DR. Encoded with physical laws and constitutive equations and integrated with neural-network training algorithms, AIV performs more effectively compared to the existing methods, particularly when the experimental data are limited. AIV also incorporates data from visual images, which is particularly important for investigation of blood flow (i.e., flow of RBCs and other blood components such as platelets) under pathological conditions where reliable constitutive laws may not be able to accurately describe hematological properties of blood for patient-specific disease states. AIV also can potentially facilitate scientific research in laboratories where systematic experiments alone, even with advanced tools, may not be sufficient to quantify all of the key parameters responsible for the pathogenesis of vascular injury. With continuous training, AIV offers a potentially powerful pathway to infer hemodynamics from in vivo examination and to develop quantitative metrics for patient diagnosis and monitoring.

Materials and Methods

Experimental Setup.

MA PDMS channel fabrication. As illustrated in Fig. 2 *A* and *B*, eight microchannels that contain various sizes of cavities are designed to mimic different MAs. The BNR of the simulated MAs is defined as the largest caliber of the MA body divided by the size of feeding vessels and varies from 12 to 1.5. These MA channels were fabricated with polydimethylsiloxane (PDMS) using standard soft lithography. Each device was fabricated by using a master mold, lithographically patterned with SU-8 negative photoresist (Microchem Corporation) on a 4-inch silicon wafer (Silicon Connection), which was later placed inside a Petri dish. Commercial thermocurable PDMS (Sylgard 184, Dowsil) prepolymer was prepared by mixing the base and curing agent at a 10:1 weight ratio, following which the PDMS prepolymers were degassed under vacuum and cast onto the mold. Thermal cross-linking of PDMS was performed by curing at 80 °C for 2 h. The cured PDMS was cut and peeled off from the channel mold, following which the inlet and outlet access ports were created by using a 1.5-mm-diameter punch. Next, the PDMS channel was bonded with a cover slide under 80 °C for 2 h. Experiments were conducted after plasma pretreatment for 1 min.

Sample preparation. Peripheral blood was drawn from a healthy donor by Venipuncture into a K2E EDTA tube, after which the whole blood was centrifuged at 200 × *g* for 12 min to extract platelet-rich plasma (PRP). The upper layer of PRP was further centrifuged at 1,200 × *g* for 5 min to acquire platelets, which were washed three times with platelet-washing solution and then resuspended in phosphate-buffered saline. The remaining blood cells were stored at 4 °C for later use. The platelets were then stained with DIOC6 (Sigma-Aldrich) (0.5 μg/mL) for 1 h at room temperature. After being washed five times, the stained platelets were remixed with the remaining blood cells from the original whole blood at a 50% hematocrit for fluorescence imaging in the MA PDMS channels. The entire process was completed within 4 h to minimize the risk of time-dependent platelet malfunction.

All procedures on peripheral blood specimens were approved and performed in accordance with the Singapore National Health Group Domain Specific Review Board (the central ethics committee) and mutually recognized by Nanyang Technological University Institutional Review Board (IRB#2018/00671). All blood specimens were de-identified prior to use in the experiment.

Microfluidics experiment and visualization. The microfluidic device was installed on a Nikon Eclipse T2000-U (Nikon) and visualized under a 40× objective. A blood sample, 20μL in volume, was loaded into a reservoir (outlet) of the PDMS channel. A negative pressure of about −5 mbar was applied to the outlet, such that the blood cells flowed from the inlet into the direction of the outlet, thus generating the flow pattern recorded by the camera. Video images were recorded by a high-speed camera, FASTCAM SA1.1 (Photron). Bright-field images (Fig. 2 *B* and *C*), which are recorded at

500 frames per second (fps) and resolved with 1 μm/pixel, served as the training data for the AIV model to infer velocity fields in microchannels. The fluorescent images (Fig. 2*D*), where the platelets or platelet aggregation were visualized as bright spots, were recorded at 60 fps, and they were used to perform cell-tracking measurements of platelets for AIV validation.

AIV Model.

Underlying physics laws. To estimate the velocity and pressure fields from a sequence of images from microfluidic experiments (Fig. 2*C*), we follow the optical flow constraint (35), a basic assumption widely used in computer vision or fluid visualization. Here, it is assumed that the variation in the image brightness represents blood flow, and the image intensity is a spatiotemporal scalar field $I(x, y, t)$, whose transport can be described by an advection equation:

$$\frac{\partial I}{\partial t} + (\mathbf{u} \cdot \nabla) I = 0, \quad [1]$$

where $\mathbf{u}$ is the 2D velocity projected onto the image plane, and ∇ is the spatial derivative operator. The fluid flow is taken to be governed by the incompressible Navier–Stokes equations:

$$\rho(\frac{\partial \mathbf{u}}{\partial t} + (\mathbf{u} \cdot \nabla)\mathbf{u}) = -\nabla p + \nabla \cdot [\mu(\nabla \mathbf{u} + (\nabla \mathbf{u})^T)], \quad \nabla \cdot \mathbf{u} = 0, \quad [2]$$

where ρ (1,060 kg/m^3) and p are the fluid density and pressure, respectively; μ is the dynamic viscosity. We also implemented the Carreau–Yasuda rheology model to capture the shear-thinning behavior of blood, which is expressed as

$$\mu(\dot{\gamma}) = \mu_0 \cdot \left[\eta_\infty + (\eta_0 - \eta_\infty)[1 + \lambda \dot{\gamma}^\alpha]^{(n-1)/a}\right], \quad [3]$$

where $\mu_0 = 3.5 \times 10^{-3}$ Pa·s is the reference viscosity; $\eta_\infty = 1$, $\eta_0 = 40$, $\lambda = 8.2$ s, $a = 0.64$ and $n = 0.2128$, all of which are parametrized for human blood (73). The shear rate, $\dot{\gamma}$, which depends on the second invariant of the stress–strain rate tensor $\mathbf{E}$, is written as

$$\dot{\gamma} = \sqrt{2\mathbf{E} : \mathbf{E}}, \quad \mathbf{E} = \frac{1}{2}(\nabla \mathbf{u} + (\nabla \mathbf{u})^T). \quad [4]$$

In order to extract relevant nondimensional parameters, we define the characteristic length as $D = 25$ μm (which is equal to the channel width) and the characteristic velocity as $U = 1$ mm/s (which is the mean velocity inside the vessel). As a result, the Reynolds number representative of the fluid flow problem considered here is $\mathrm{Re} \approx 7 \times 10^{-3}$.

Integrating physics with image data from microfluidic experiments using AIV. The AIV technique employed here is based on PINNs, which were originally developed for solving forward and inverse problems for partial differential equations (47, 74) and were subsequently extended to solve fluid-mechanics problems (48, 75–77). AIV is capable of seamlessly assimilating the Navier–Stokes equations and the experimental data, and thus allows for the extraction of velocity and pressure fields by considering both the underlying physics of blood flow and the microfluidics or in vivo image data. As shown in Fig. 1, AIV contains a fully connected neural network, which is used to approximate the solutions, i.e., $(I, \mathbf{u}, p) = \mathcal{F}_{NN}(\mathbf{x}, t)$. This neural network takes the coordinates and time as inputs and provides as outputs the corresponding image intensity, velocity, and pressure. As the image intensity in the spatiotemporal domain $I(\mathbf{x}, t)$ can be obtained from the image data, the loss function of the neural network can be defined as

$$\mathcal{L}_{data} = \frac{1}{N_d} \sum_{i=1}^{N_d} \| I_{data}(\mathbf{x}_i, t_i) - I_{NN}(\mathbf{x}_i, t_i) \|, \quad [5]$$

where I_{data} and I_{NN} are the data from visual images and the output of neural network, respectively; and N_d is the number of pixels in the investigated domain. In addition to loss from the mismatch between image data and neural-network predictions ($\mathcal{L}_{data}$), AIV introduces a residual loss ($\mathcal{L}_{res}$) resulting from computing the residuals of the governing equations (Eq. **2**) on random points to take into account the underlying physics of blood flow. $\mathcal{L}_{res}$ is expressed as:

$$\mathcal{L}_{res} = \frac{1}{N_e} \sum_{i=1}^{N_e} \sum_{j=1}^{5} \| e_j(\mathbf{x}_i, t_i) \|, \quad [6]$$

where N_e is the number of residual points $(\mathbf{x}_i, t_i)$ for evaluating the equations, which can be selected in the computational domain based on the location of interest. The no-slip boundary conditions on the channel walls are enforced by adding another loss term:

$$\mathcal{L}_{bcs} = \frac{1}{N_b} \sum_{i=1}^{N_b} \| \mathbf{u}(\partial\Omega) \|, \quad [7]$$

where $\partial\Omega$ denotes the boundaries of the channel wall; N_b is the total number of pixels on the boundary. As a result, the parameters of the AIV model are obtained by minimizing the following total loss function:

$$\mathcal{L} = \lambda_d \mathcal{L}_{data} + \lambda_b \mathcal{L}_{bcs} + \mathcal{L}_{res}, \quad [8]$$

where λ_d and λ_b are the weighing coefficients to account for the relative contributions of the three terms in the total loss function. We note that for AIV, using large values of λ_d and λ_b can accelerate the optimization because the image data can be quickly regressed, but it may also result in overfitting. More details of how to select the appropriate weighing coefficients in the loss function for training PINNs can be found in refs. 76 and 77. In our simulations, we chose $\lambda_d = 10$ and $\lambda_b = 100$ through a trial-and-run process. Details of the selection of these parameters can be found in *SI Appendix*. We train the network using the Adam optimizer (78), an adaptive algorithm for gradient-based, first-order optimization of stochastic objective functions. Once the training is accomplished, the AIV model can infer the full solutions of $(I, \mathbf{u}, p)$ at any given point $(\mathbf{x}, t)$ inside the computational domain and compute the shear rate and wall shear stress. More details of the hyperparameters of the AIV model and the training strategy can be found in *SI Appendix*.

Data Availability. The data and codes used in this manuscript are publicly available on GitHub (https://github.com/shengzesnail/AIV_MAOAC) (79).

ACKNOWLEDGMENTS. S.C. and G.E.K. were supported by Department of Energy Physics-Informed Learning Machines Project No. DE-SC0019453. H.L., M.D., and G.E.K. were supported by NIH Grant R01HL154150. M.D. was supported by the Massachusetts Institute of Technology J-Clinic for Machine Learning and Health. F.K. and S.S. were supported by Nanyang Technological University, Singapore, through the Distinguished University Professorship (S.S.).

1. H. H. Lipowsky, Microvascular rheology and hemodynamics. *Microcirculation* **12**, 5–15 (2005).
2. A. S. Popel, P. C. Johnson, Microcirculation and hemorheology. *Annu. Rev. Fluid Mech.* **37**, 43–69 (2005).
3. T. W. Secomb, Blood flow in the microcirculation. *Annu. Rev. Fluid Mech.* **49**, 443–461 (2017).
4. C. A. Taylor, J. Humphrey, Open problems in computational vascular biomechanics: Hemodynamics and arterial wall mechanics. *Comput. Methods Appl. Mech. Eng.* **198**, 3514–3523 (2009).
5. A. M. Nixon, M. Gunel, B. E. Sumpio, The critical role of hemodynamics in the development of cerebral vascular disease: A review. *J. Neurosurg.* **112**, 1240–1253 (2010).
6. D. J. Green, M. T. Hopman, J. Padilla, M. H. Laughlin, D. H. Thijssen, Vascular adaptation to exercise in humans: Role of hemodynamic stimuli. *Physiol. Rev.* **97**, 495–528 (2017).
7. J. Sagel, J. A. Colwell, L. Crook, L. Marta, Increased platelet aggregation in early diabetes mellitus. *Ann. Intern. Med.* **82**, 733–738 (1975).
8. S. P. Jackson, The growing complexity of platelet aggregation. *Blood* **109**, 5087–5095 (2007).
9. D. Kaiser, M. A. Freyberg, P. Friedl, Lack of hemodynamic forces triggers apoptosis in vascular endothelial cells. *Biochem. Biophys. Res. Commun.* **231**, 586–590 (1997).
10. M. A. Gimbrone Jr, J. N. Topper, T. Nagel, K. R. Anderson, G. Garcia-Cardeña, Endothelial dysfunction, hemodynamic forces, and atherogenesis[a]. *Ann. N. Y. Acad. Sci.* **902**, 230–240 (2000).
11. L. D. Casa, D. H. Deaton, D. N. Ku, Role of high shear rate in thrombosis. *J. Vasc. Surg.* **61**, 1068–1080 (2015).
12. C. C. Kwan, A. A. Fawzi, Imaging and biomarkers in diabetic macular edema and diabetic retinopathy. *Curr. Diabetes Rep.* **19**, 95 (2019).
13. Y. W. Choo, J. Jeong, K. Jung, Recent advances in intravital microscopy for investigation of dynamic cellular behavior in vivo. *BMB Rep.* **53**, 357 (2020).
14. E. Courtie, T. Veenith, A. Logan, A. Denniston, R. Blanch, Retinal blood flow in critical illness and systemic disease: A review. *Ann. Intensive Care* **10**, 1–18 (2020).
15. T. Omori, Y. Imai, K. Kikuchi, T. Ishikawa, T. Yamaguchi, Hemodynamics in the microcirculation and in microfluidics. *Ann. Biomed. Eng.* **43**, 238–257 (2015).

16. S. M. Hastings, M. T. Griffin, D. N. Ku, Hemodynamic studies of platelet thrombosis using microfluidics. *Platelets* **28**, 427–433 (2017).
17. B. A. Herbig, X. Yu, S. L. Diamond, Using microfluidic devices to study thrombosis in pathological blood flows. *Biomicrofluidics* **12**, 042201 (2018).
18. B. Sebastian, P. S. Dittrich, Microfluidics to mimic blood flow in health and disease. *Annu. Rev. Fluid Mech.* **50**, 483–504 (2018).
19. J. G. Santiago, S. T. Wereley, C. D. Meinhart, D. Beebe, R. J. Adrian, A particle image velocimetry system for microfluidics. *Exp. Fluid* **25**, 316–319 (1998).
20. C. D. Meinhart, S. T. Wereley, J. G. Santiago, PIV measurements of a microchannel flow. *Exp. Fluid* **27**, 414–419 (1999).
21. S. T. Wereley, L. Gui, C. Meinhart, Advanced algorithms for microscale particle image velocimetry. *AIAA J.* **40**, 1047–1055 (2002).
22. J. S. Raben, S. A. Klein, J. D. Posner, P. P. Vlachos, Improved accuracy of time-resolved micro-particle image velocimetry using phase-correlation and confocal microscopy. *Microfluid. Nanofluidics* **14**, 431–444 (2013).
23. C. J. Kähler *et al.*, Main results of the 4th International PIV Challenge. *Exp. Fluid* **57**, 97 (2016).
24. R. Lindken, M. Rossi, S. Große, J. Westerweel, Micro-particle image velocimetry (μPIV): Recent developments, applications, and guidelines. *Lab Chip* **9**, 2551–2567 (2009).
25. S. J. Williams, C. Park, S. T. Wereley, Advances and applications on microfluidic velocimetry techniques. *Microfluid. Nanofluid.* **8**, 709–726 (2010).
26. S. T. Wereley, C. D. Meinhart, Recent advances in micro-particle image velocimetry. *Annu. Rev. Fluid Mech.* **42**, 557–576 (2010).
27. R. Lima, T. Ishikawa, Y. Imai, T. Yamaguchi, "Blood flow behavior in microchannels: Past, current and future trends" in *Single and Two-Phase Flows on Chemical and Biomedical Engineering*, R. Dias, A. A. Martins, R. Lima, T. M. Mata, Eds. (Bentham Science, Sharjah, United Arab Emirates, 2012), pp. 513–547.
28. K. Pitts, R. Mehri, C. Mavriplis, M. Fenech, Micro-particle image velocimetry measurement of blood flow: Validation and analysis of data pre-processing and processing methods. *Meas. Sci. Technol.* **23**, 105302 (2012).
29. R. Lima *et al.*, In vitro blood flow in a rectangular PDMS microchannel: Experimental observations using a confocal micro-PIV system. *Biomed. Microdevices* **10**, 153–167 (2008).
30. F. Champagnat *et al.*, Fast and accurate PIV computation using highly parallel iterative correlation maximization. *Exp. Fluid* **50**, 1169 (2011).
31. J. Rabault, J. Kolaas, A. Jensen, Performing particle image velocimetry using artificial neural networks: A proof-of-concept. *Meas. Sci. Technol.* **28**, 125301 (2017).
32. S. Cai, J. Liang, Q. Gao, C. Xu, R. Wei, Particle image velocimetry based on a deep learning motion estimator. *IEEE Trans. Inst. Measur.* **69**, 3538–3554 (2020).
33. B. Horn, B. Schunck, Determining optical flow. *Artif. Intell.* **17**, 185–203 (1981).
34. T. Corpetti, D. Heitz, G. Arroyo, E. Mémin, A. Santa-Cruz, Fluid experimental flow estimation based on an optical-flow scheme. *Exp. Fluid* **40**, 80–97 (2006).
35. T. Liu, L. Shen, Fluid flow and optical flow. *J. Fluid Mech.* **614**, 253–291 (2008).
36. D. Heitz, E. Mémin, C. Schnörr, Variational fluid flow measurements from image sequences: Synopsis and perspectives. *Exp. Fluid* **48**, 369–393 (2010).
37. G. Gompper, D. A. Fedosov, Modeling microcirculatory blood flow: Current state and future perspectives. *Wiley Interdis. Rev. Syst. Biol. Med.* **8**, 157–168 (2016).
38. J. O'Connor, P. Day, P. Mandal, A. Revell, Computational fluid dynamics in the microcirculation and microfluidics: What role can the lattice Boltzmann method play? *Integr. Biol.* **8**, 589–602 (2016).
39. E. Westein *et al.*, Atherosclerotic geometries exacerbate pathological thrombus formation poststenosis in a von Willebrand factor-dependent manner. *Proc. Natl. Acad. Sci. U.S.A.* **110**, 1357–1362 (2013).
40. A. Yazdani, H. Li, J. D. Humphrey, G. E. Karniadakis, A general shear-dependent model for thrombus formation. *PLoS Comput. Biol.* **13**, e1005291 (2017).
41. L. Mountrakis, E. Lorenz, A. Hoekstra, Where do the platelets go? A simulation study of fully resolved blood flow through aneurysmal vessels. *Interf. Focus* **3**, 20120089 (2013).
42. M. O. Bernabeu, Y. Lu, O. Abu-Qamar, L. P. Aiello, J. K. Sun, Estimation of diabetic retinal microaneurysm perfusion parameters based on computational fluid dynamics modeling of adaptive optics scanning laser ophthalmoscopy. *Front. Physiol.* **9**, 989 (2018).
43. Y. Lu *et al.*, Computational fluid dynamics assisted characterization of parafoveal hemodynamics in normal and diabetic eyes using adaptive optics scanning laser ophthalmoscopy. *Biomed. Optic Express* **7**, 4958–4973 (2016).
44. P. Perdikaris, L. Grinberg, G. E. Karniadakis, Multiscale modeling and simulation of brain blood flow. *Phys. Fluids* **28**, 021304 (2016).
45. S. Sankaran, A. L. Marsden, A stochastic collocation method for uncertainty quantification and propagation in cardiovascular simulations. *J. Biomech. Eng.* **133** (2011).
46. M. Abadi et al., "Tensorflow: A system for large-scale machine learning" in *12th USENIX Symposium on Operating Systems Design and Implementation (OSDI 16)* (USENIX Association, Berkeley, CA, 2016), pp. 265–283.
47. M. Raissi, P. Perdikaris, G. E. Karniadakis, Physics-informed neural networks: A deep learning framework for solving forward and inverse problems involving nonlinear partial differential equations. *J. Comput. Phys.* **378**, 686–707 (2019).
48. M. Raissi, A. Yazdani, G. E. Karniadakis, Hidden fluid mechanics: Learning velocity and pressure fields from flow visualizations. *Science* **367**, 1026–1030 (2020).
49. D. Fedosov, B. Caswell, S. Suresh, G. Karniadakis, Quantifying the biophysical characteristics of plasmodium-falciparum-parasitized red blood cells in microcirculation. *Proc. Natl. Acad. Sci. U.S.A.* **108**, 35–39 (2011).
50. E. Ruckenstein, P. Rajora, On the no-slip boundary condition of hydrodynamics. *J. Colloid Interface Sci.* **96**, 488–491 (1983).
51. H. Guha, T. Chaudhury, Flow in an arteriosclerotic blood vessel with rigid permeable wall. *Bull. Math. Biol.* **47**, 613–627 (1985).
52. J. Misra, G. Shit, Role of slip velocity in blood flow through stenosed arteries: A non-Newtonian model. *J. Mech. Med. Biol.* **7**, 337–353 (2007).
53. D. S. W. Ting, G. C. M. Cheung, T. Y. Wong, Diabetic retinopathy: Global prevalence, major risk factors, screening practices and public health challenges: A review. *Clin. Exp. Ophthalmol.* **44**, 260–277 (2016).
54. M. Dubow *et al.*, Classification of human retinal microaneurysms using adaptive optics scanning light ophthalmoscope fluorescein angiography. *Invest. Ophthalmol. Vis. Sci.* **55**, 1299–1309 (2014).
55. V. Schreur *et al.*, Morphological and topographical appearance of microaneurysms on optical coherence tomography angiography. *Br. J. Ophthalmol.* **103**, 630–635 (2019).
56. S. Cai *et al.*, "Deep-PIV: A new framework of PIV using deep learning techniques" in *13th International Symposium on Particle Image Velocimetry: ISPIV 2019*, C. J. Kähler, R. Hain, S. Scharnowski, T. Fuchs, Eds. (Universität der Bundeswehr, Munich, Germany, 2019).
57. G. Karniadakis, S. Sherwin, *Spectral/hp Element Methods for Computational Fluid Dynamics* (Oxford University Press, Oxford, UK, 2013).
58. H. Y. Chang *et al.*, Quantifying platelet margination in diabetic blood flow. *Biophys. J.* **115**, 1371–1382 (2018).
59. E. Ezra, E. Keinan, Y. Mandel, M. E. Boulton, Y. Nahmias, Non-dimensional analysis of retinal microaneurysms: Critical threshold for treatment. *Integr. Biol.* **5**, 474–480 (2013).
60. L. Boussel *et al.*, Aneurysm growth occurs at region of low wall shear stress: Patient-specific correlation of hemodynamics and growth in a longitudinal study. *Stroke* **39**, 2997–3002 (2008).
61. R. Fahraeus, T. Lindqvist, The viscosity of the blood in narrow capillary tubes. *Amm. J. Physiol. Leg. Cont.* **96**, 562–568 (1931).
62. P. Aarts *et al.*, Blood platelets are concentrated near the wall and red blood cells, in the center in flowing blood. *Arteriosclerosis* **8**, 819–824 (1988).
63. R. Zhao, M. V. Kameneva, J. F. Antaki, Investigation of platelet margination phenomena at elevated shear stress. *Biorheology* **44**, 161–177 (2007).
64. A. Kumar, M. D. Graham, Margination and segregation in confined flows of blood and other multicomponent suspensions. *Soft Matter* **8**, 10536–10548 (2012).
65. H. Li *et al.*, Predictive modelling of thrombus formation in diabetic retinal microaneurysms. *R. Soc. Open Sci.* **7**, 201102 (2020).
66. A. Stitt, T. Gardiner, D. Archer, Histological and ultrastructural investigation of retinal microaneurysm development in diabetic patients. *Br. J. Ophthalmol.* **79**, 362–367 (1995).
67. R. Lindken, J. Westerweel, B. Wieneke, Stereoscopic micro particle image velocimetry. *Exp. Fluid* **41**, 161–171 (2006).
68. S. Satake *et al.*, Measurements of 3D flow in a micro-pipe via micro digital holographic particle tracking velocimetry. *Meas. Sci. Technol.* **17**, 1647 (2006).
69. X. Meng, G. E. Karniadakis, A composite neural network that learns from multi-fidelity data: Application to function approximation and inverse PDE problems. *J. Comput. Phys.* **401**, 109020 (2020).
70. L. Lu *et al.*, Extraction of mechanical properties of materials through deep learning from instrumented indentation. *Proc. Natl. Acad. Sci. U.S.A.* **117**, 7052–7062 (2020).
71. J. Donea, S. Giuliani, J. P. Halleux, An arbitrary Lagrangian-Eulerian finite element method for transient dynamic fluid-structure interactions. *Comput. Methods Appl. Mech. Eng.* **33**, 689–723 (1982).
72. H. H. Hu, N. A. Patankar, M. Zhu, Direct numerical simulations of fluid–solid systems using the arbitrary Lagrangian–Eulerian technique. *J. Comput. Phys.* **169**, 427–462 (2001).
73. J. Boyd, J. M. Buick, S. Green, Analysis of the Casson and Carreau-Yasuda non-Newtonian blood models in steady and oscillatory flows using the lattice Boltzmann method. *Phys. Fluids* **19**, 093103 (2007).
74. L. Lu, X. Meng, Z. Mao, G. E. Karniadakis, DeepXDE: A deep learning library for solving differential equations. *SIAM Rev.*, **63**, 208–228 (2021).
75. M. Raissi, Z. Wang, M. S. Triantafyllou, G. E. Karniadakis, Deep learning of vortex-induced vibrations. *J. Fluid Mech.* **861**, 119–137 (2019).
76. X. Jin, S. Cai, H. Li, G. E. Karniadakis, NSFnets (Navier-Stokes flow nets): Physics-informed neural networks for the incompressible Navier-Stokes equations. *J. Comput. Phys.* **426**, 109951 (2021).
77. S. Wang, Y. Teng, P. Perdikaris, Understanding and mitigating gradient pathologies in physics-informed neural networks. arXiv [Preprint] (2020) https://arxiv.org/abs/2001.04536 (Accessed 13 January 2020).
78. D. P. Kingma, J. Ba, Adam: A method for stochastic optimization. arXiv [Preprint] (2017) https://arxiv.org/abs/1412.6980 (Accessed 30 January 2017).
79. S. Cai *et al.*, AIV MAOAC. GitHub. https://github.com/shengzesnail/AIV_MAOAC. Deposited 4 February 2021.

PNAS
www.pnas.org

Supplementary Information for

Artificial intelligence velocimetry and microaneurysm-on-a-chip for three-dimensional analysis of blood flow in physiology and disease

Shengze Cai, He Li, Fuyin Zheng, Fang Kong, Ming Dao, George Em Karniadakis and Subra Suresh

Corresponding authors: Ming Dao, George Em Karniadakis, Subra Suresh
E-mail: mingdao@mit.edu, george_karniadakis@brown.edu, ssuresh@ntu.edu.sg

This PDF file includes:

Supplementary text
Figs. S1 to S5 (not allowed for Brief Reports)
Tables S1 to S4 (not allowed for Brief Reports) SI
References

Other supplementary materials for this manuscript include the following:

Movies S1 and S2

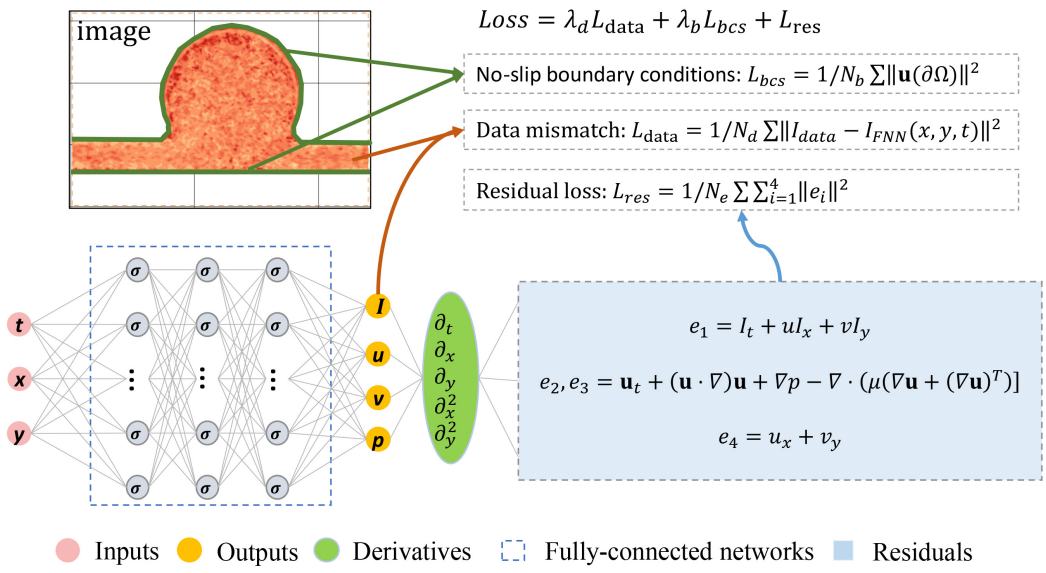

Fig. S1. Schematic diagram of 2D AIV model. A fully-connected network is used to approximate the key output parameters, namely (I, u, v, p), by taking the space and time coordinates as inputs (x, y, t). The governing equations for this problem are encoded in a residual network, where the derivatives are computed via automatic differentiation (AD) in the TensorFlow code (Google, Mountain View, CA, USA). Moreover, the no-slip boundary conditions are introduced on the channel walls (denoted by green lines at the top-left image), namely $\mathbf{u}(\partial\Omega) = 0$. The activation function for each neuron is $\sigma(\cdot) = \sin(\cdot)$. The loss function for training is composed of three terms: data mismatch, boundary conditions and residuals of conservation laws.

Table S1. Number of training data points used for training of 2D AIV. N_d represents the number of training data from microfluidic images. N_e denotes the number of training points for computing the residues of the governing equations. N_b designates the number of training points on the channel wall.

MA	MA#3	MA#4	MA#6
N_d	7410	10353	14983
N_b	510	522	587
N_e	7410	10353	14983

Supporting Information Text

1. Implementation details of AIV

2D AIV model. The details of the AIV model employed to infer the 2D velocity and pressure fields from 2D images is elaborated in Fig. S1. The inputs (purple circles) to the model are the time and 2D spatial coordinates (t, x, y) and the outputs of the model (orange circles) are spatio-temporal scalar field I which represents the image intensity as well as the 2D velocity and pressure field (u, v, p). The encoded equations in the AIV model (in the blue box) include the image advection equation, the 2D Navier-Stokes equation and continuity equation.

Training data. The training data sets for AIV include (1) the data points extracted from the microfluidic images $\{\mathbf{x}_i, t_i, I_i\}_{i=1}^{N_d \times N_t}$ for computing $\mathcal{L}_{data}$; (2) the residual points $\{\mathbf{x}_i, t_i\}_{i=1}^{N_e \times N_t}$ used in the governing equations for computing $\mathcal{L}_{res}$; and (3) the points selected on the boundaries of the channel wall $\{\mathbf{x}_i, t_i\}_{i=1}^{N_b \times N_t}$ for computing $\mathcal{L}_{bcs}$, where N_t denotes the number of image frames. The number of data points N_d and the number of points on the wall boundary N_b are selected based on the number of pixels in the microfluidic images, while N_e is selected to be $N_e = N_d$ for the prediction of 2D velocity and pressure fields. The values of N_d, N_b and N_e used for the three MAOAC channels with different geometries are listed in Table S1. 100 sequential images (i.e., $N_t = 100$) are extracted from the blood flow videos for each of these three MAOAC channels to train AIV.

Hyperparameters. As illustrated in Fig. S1, the AIV model is composed of a fully-connected network containing 10 hidden layers with 80 neurons per layer. For each layer, the input-output relationship can be expressed as: $Y = \sigma(WX + b)$, where W and b are the trainable weights and biases, respectively. The activation function for each neuron is $\sigma(\cdot) = \sin(\cdot)$. All the weights and biases are randomly initialized by the Xavier scheme (1). The training of the network is performed using *Adam* optimizer (2). In order to calculate the residuals (e_1,e_2,e_3 and e_4 in Fig. S1) in $\mathcal{L}_{res}$, the partial differential operators in the governing equations are computed using automatic differentiation (AD) where the derivatives in the governing equations are

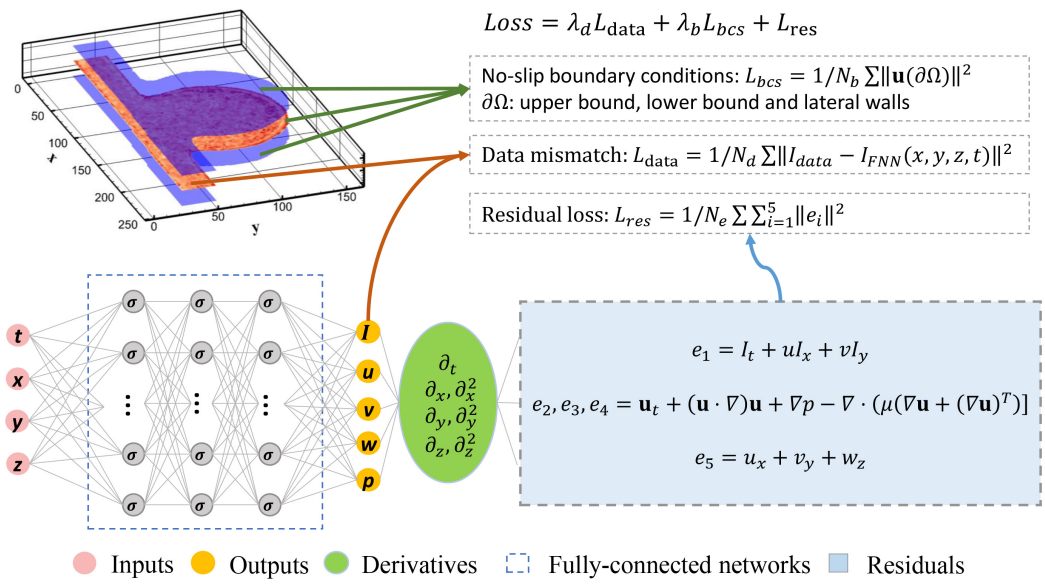

Fig. S2. Schematic diagram of 3D AIV model. A fully-connected network is used to approximate the solutions, namely (I, u, v, w, p), by taking the space and time coordinates as inputs (x, y, z, t). The governing equations include the transport equation of image intensity, the three-component momentum equations and the continuity equation.

approximated by the derivatives of the output with respect to the input of the neural networks. λ_d and λ_b are the weighing coefficients to account for the relative contributions of the three terms in the total loss function. We note that for AIV, a relatively large λ_d and λ_b can accelerate optimization because the image data can be quickly regressed, but it may also result in overfitting. More details of how to select the appropriate weighing coefficients in the loss function for training PINNs can be found in (3, 4). In this work, the weighting coefficient for L_{data} is selected to be $\lambda_d = 10$ through a trial-and-run process. As we impose no-slip boundary conditions on the channel wall, we implement a stronger penalization ($\lambda_b = 100$) on loss resulting from the boundary conditions (L_{bcs}) to constrain the magnitude of the velocity on the channel wall to be approximately zero.

Training strategy. The training of AIV are performed using a two-step optimization. In the first step, we train the network with 5,000 epochs with initial learning rate 10^{-3} and we observe that the total loss function has reached a plateau. One epoch in the training means that all the selected training points ($N_d + N_b + N_c$ in Table S1) have been used to train the neural network once. In this step, L_{data} are predominately minimized through the optimization process such that the AIV model can attain a good regression to the microfluidic image data. Next, we exclude the data term (L_{data}) as well as the image advection equation (residual e_1) in the loss function, and train the neural network for another 50000 epochs with a smaller learning rate (10^{-4}) to fine-tune the velocity and pressure fields based on the residuals of Navier–Stokes (NS) equations.

3D AIV model. The 3D AIV model, as shown in Fig. S2, is composed of a neural network containing 10 layers with 100 neurons per layer. The training points for the residual loss (L_{res}) are selected uniformly in the 3D computational domain as illustrated in Fig.7(A) in the maintext. We select the number of training points for computing the residues of the governing equations, $N_e = 2N_d$, where N_d is the number of 2D image pixels. The number of training points on the channel wall N_b is selected to be 50000 for the 3D case and they are uniformly distributed on the upper bound, lower bound and lateral channel walls. We train the 3D AIV following the same strategy as introduced in the 2D AIV model.

2. Methods for comparisons

Variational optical flow. Variational optical flow is one of the most popular techniques in the computer vision community for estimation of the movement of objects in a sequence of images (5–7). The estimation of flow field is performed by minimizing an objective function which is expressed as

$$\min_{\mathbf{u}} J = \int_{\Omega} \left[(\partial_t I + \nabla I \cdot \mathbf{u})^2 + \alpha \parallel \nabla \mathbf{u} \parallel^2 \right] d\Omega. \quad [1]$$

The first term in the function considers the data extracted from the sequential images under the assumption that the targeted objects have the fixed brightness in the sequential images. The second term is a regularization term for smoothing the velocity field. The optical flow-based methods have been developed for fluid flow motion estimation, especially for PIV (8–10). In this work, we implement the multi-resolution algorithm (10) to solve Eq. 1. The algorithm and the corresponding code can be found at: https://github.com/shengzesnail/coarse_to_fine_HS_PIV. The weighting coefficient α is 100 and the result is obtained by taking the average of 100 instances.

Deep-PIV. Deep-PIV, designed for particle image velocimetry, is a deep convolutional neural network with an encoder-decoder architecture (11, 12). The original Deep-PIV model was trained using thousands of particle images and the estimation of the flow field relies on the correlation of the particle positions at two consecutive images (11). In the current work, we employ the pretrained Deep-PIV model in (11) to predict the velocity field in MAOAC channels without further training because the motion of blood cells in the blood flow is analogous to particle motion. The algorithm and the corresponding code can be found at: https://github.com/shengzesnail/PIV-LiteFlowNet-en. The result of Deep-PIV is obtained by taking the average of 100 instances.

3. Modeling the transport of RBCs and platelets in the microchannel using dissipative particle dynamics

We perform dissipative particle dynamics (DPD) simulations to model the transport of red blood cells (RBCs) and platelets in channel MA#3 (BNR = 3.6), as shown in Fig. 6 in the main paper. The DPD method is a mesoscopic particle-based simulation technique, where each DPD particle represents a cluster of molecules and it interacts with other DPD particles through soft pairwise forces (13, 14). DPD method is capable of capturing the hydrodynamic behavior of fluids at the mesoscale, and it has been successfully employed to study complex fluids, such as blood (15, 16). The equation of motion for each DPD particle i is governed by the sum of pair interactions $\mathbf{f}_i$ with the surrounding particles j. The time evolution of velocity ($\mathbf{v}_i$) and position ($\mathbf{r}_i$) of a particle i with mass m_i is determined by Newton's second law of motion:

$$\mathrm{d}\mathbf{r}_i = \mathbf{v}_i\,\mathrm{d}t\,; \quad \mathrm{d}\mathbf{v}_i = \mathbf{f}_i/m_i\,\mathrm{d}t. \tag{2}$$

where dt is the simulation timestep size. These two equations of motion of DPD particles are solved using a velocity-Verlet algorithm. In the classical DPD method (13, 14), the total force $\mathbf{f}_i$ exerted on particle i by particle j is composed of a conservative force ($\mathbf{F}^C_{ij}$), a dissipative force ($\mathbf{F}^D_{ij}$), and a random force ($\mathbf{F}^R_{ij}$) given by

$$\mathbf{F}^C_{ij} = a_{ij}(1-\frac{r_{ij}}{r_c})\hat{\mathbf{r}}_{ij} \quad for \quad r_{ij} \le r_c; \quad 0 \quad for \quad r_{ij} > r_c, \tag{3}$$

$$\mathbf{F}^D_{ij} = \gamma\omega_d(r_{ij})(\hat{\mathbf{r}}_{ij}\cdot\hat{\mathbf{v}}_{ij})\hat{\mathbf{r}}_{ij}, \tag{4}$$

$$\mathbf{F}^R_{ij} = \sigma\omega_r(r_{ij})\frac{\zeta_{ij}}{\sqrt{dt}}\hat{\mathbf{r}}_{ij}, \tag{5}$$

where r_c is a cut-off distance beyond which the interaction force is considered to be zero. a_{ij}, γ, σ are the conservative, dissipative and random coefficients, respectively. The DPD parameters used in Eqs. (3)-(5) for all types of DPD particles are given in Table.S2. r_{ij} is the distance between particle i and j. $\hat{\mathbf{r}}_{ij}$ is a unit vector. $\hat{\mathbf{v}}_{ij}$ is the difference between the $\mathbf{v}_i$ and $\mathbf{v}_j$. ζ_{ij} is a Gaussian random number with zero mean and unit variance. The parameters γ and σ and the weight functions are coupled through the fluctuation-dissipation theorem and are related by $\omega_d = \omega_r^2$ and $\sigma^2 = 2\gamma k_B T$, where k_B is the Boltzmann constant and T is the temperature of the system. The weight function $\omega_r(r_{ij}) = (1-r_{ij}/r_c)^k$ with $k = 1$ in the standard DPD method (13, 14), whereas other values of k have been used to increase the fluid viscosity (15, 17, 18). More detailed description of DPD method can be found in (13, 19).

In addition to blood plasma modeled by collections of free DPD particles, the membrane of blood cells suspended in the plasma, including RBCs and platelets, is constructed by a 2D triangulated network with N_v vertices (DPD particles). The vertices are connected by N_s elastic bonds to impose proper membrane mechanics. These DPD representations of RBCs and platelets were validated and widely used in the previous studies for both healthy and diseased cells (18, 20–22). The free energy V_{cell} of a single cell is given by

$$V_{cell} = V_s + V_b + V_{a+v}. \tag{6}$$

The elastic energy V_s representing the elastic interactions of the cell membrane is defined by

$$V_s = \sum_{j\in 1\ldots N_s}\left[\frac{k_{\mathrm{B}}Tl_m(3x_j^2-2x_j^3)}{4p(1-x_j)} + \frac{k_p}{l_j}\right], \tag{7}$$

where p is the persistence length, k_p is the spring constant, $k_{\mathrm{B}}T$ is the energy unit, l_j is the length of the spring j, l_m is the maximum spring extension, and $x_j = l_j/l_m$. p and k_p are computed by balancing the forces at equilibrium and from their relation to the macroscopic shear modulus, μ_s:

$$\mu_s = \frac{\sqrt{3}k_{\mathrm{B}}T}{4pl_mx_0}\left(\frac{x_0}{2(1-x_0)^3} - \frac{1}{4(1-x_0)^2} + \frac{1}{4}\right) + \frac{3\sqrt{3}k_p}{4l_0^3}, \tag{8}$$

where l_0 is the equilibrium spring length and $x_0 = l_0/l_m$. The bending resistance V_b of the cell membrane is modeled by

$$V_b = \sum_{j\in 1\ldots N_s} k_b\left[1-cos(\theta_j-\theta_0)\right], \tag{9}$$

where k_b is the bending constant, and it is related to the macroscopic bending rigidity k_c where $k_b = 2k_c/\sqrt{3}$, θ_j is the instantaneous angle between two adjacent triangles having the common edge j, and θ_0 is the spontaneous angle. In addition,

Table S2. DPD parameters used in simulations. r_c **is a cut-off radius,** a_{ij} **is the conservative coefficient,** γ **is the dissipative coefficient, and** k **is the weight function exponent. In all simulations, we set the particle mass** $m = 1$**, and the thermal energy** $k_BT = 0.10$ **in DPD units. Note that S = solvent (representing plasma), R = RBC and P = platelet.**

type	r_c	a_{ij}	γ	k
S-S	1.58	5.0	20.0	0.20
S-R	1.5	0.0	45.0	0.20
S-P	1.5	0.0	10.0	0.20
R-R	1.0	10.0	10.0	0.20
R-P	1.0	10.0	10.0	0.20
P-P	1.0	10.0	10.0	0.20

Table S3. Cell membrane parameters for RBC and platelet models. N_v **is the number of DPD particles on the membrane,** l_m **is the maximum bond extension,** l_0 **is the equilibrium bond length,** k_b **is the bending constant,** μ_s **is the shear modulus,** $A_0^{\mathbf{tot}}$ **and** $V_0^{\mathbf{tot}}$ **are the specified cell area and volume, respectively,** $k_d + k_a$ **is the combined area constraint coefficient, and** k_v **is the volume constraint coefficient.**

cell	N_v	l_m/l_0	k_b	μ_s	A_0^{tot} (V_0^{tot})	$k_d + k_a$ (k_v)
RBC	500	1.8	6.025	100.0	132.87 (92.45)	5000 (5000)
PLT	48	1.8	100.0	10^4	19.63 (6.02)	5000 (10^4)

the area and volume constraints V_{a+v} are imposed to mimic the area-preserving lipid bilayer and the incompressible interior fluid. The corresponding energy is given by

$$V_{a+v} = \sum_{j\in 1\dots N_t} \frac{k_d(A_j - A_0)^2}{2A_0} + \frac{k_a(A_{\text{cell}} - A_0^{\text{tot}})^2}{2A_0^{\text{tot}}} + \frac{k_v(V_{\text{cell}} - V_0^{\text{tot}})^2}{2V_0^{\text{tot}}}, \quad [10]$$

where N_t is the number of triangles in the membrane network, A_0 is the equilibrium value of a triangle area, and k_d, k_a and k_v are the local area, global area and volume constraint coefficients, respectively. The terms A_0^{tot} and V_0^{tot} are targeted cell area and volume. The cell membrane parameters used in Eqs (7)-(10) for all blood cell models are given in Tables S2 and S3, respectively.

In order to prevent cell overlap, we employ a Morse potential between membrane particles from different blood cells and it is expressed as

$$V_M(r) = D_e[e^{2\beta(r_0-r)} - 2e^{\beta(r_0-r)}], \quad [11]$$

where r and r_0 are the distance and equilibrium distance between two membrane particles, respectively. D_e is the well-depth of the potential, and β characterizes the interaction range. By properly setting the parameters, we can ensure sufficiently strong repulsive forces between cell membrane particles and prevent their overlap. We present the Morse potential parameters used for cell-cell interactions in Table S4. Note that the cutoff radius $r_{c,morse} = 1$ for all the Morse interactions is given.

To drive blood flow in the microchannel, we apply a constant body force to each DPD particle and we tune this body force such that the velocity of the solvent particles around the centerline of the post-aneurysm channel, as shown in Fig.6(C) in the maintext, is close to the maximum velocity of 1.65 mm/s in the channel inferred by AIV.

In order to convert the DPD units to the physical units, we define the length scale of the simulation as $[L] = 1 \times 10^{-6}m$. Then, the time scale of the system can be evaluated by

$$[t] = [L]\frac{\eta^P}{\eta^M}\frac{\mu_s^M}{\mu_s^P} \quad [12]$$

where μ_s is the RBC membrane shear modulus, η is the plasma viscosity, and superscripts M and P denote the model (DPD) and physical units, respectively. Using membrane shear modulus of healthy RBCs $\mu_s^p = 4.73 \times 10^{-6}N/m$ and plasma viscosity $\eta^P = 1.2 \times 10^3 Pas$, the length scale is computed to be $[t] = 2.27 \times 10^{-4}s$.

4. 3D results of AIV for microchannel MA#6

The AIV prediction and the CFD simulation results of shear stress for MA#6 (BNR = 5) along two lines on two different planes in the channel depth direction are shown in Fig. S3.

Table S4. Morse potential parameters for cell-cell interactions. D_e **is the well depth of the potential,** r_0 **is the zero force distance, and** β **characterizes the interaction range. Note that R = RBC and P = platelet**

type	D_e	β	r_0
R-R	5.0	2.0	0.95
R-P	10.0	2.0	1.0
P-P	10.0	2.0	1.0

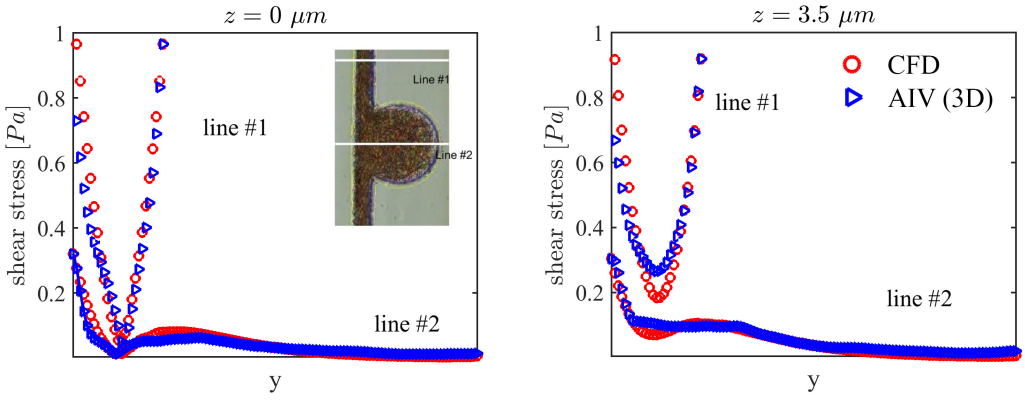

Fig. S3. Comparison between the AIV prediction and the CFD simulation of wall shear stress for MA#6 (BNR = 5) along two lines on two different planes in the channel depth direction. Left: z = 0 μm, right: z = 3.5 μm. Red circles: CFD results, blue triangles: AIV results.

5. 3D results of AIV for microchannel MA#3

We also employ 3D AIV model to predict the velocity field, pressure field and wall shear stress for MAOAC channel with BNR = 2 and the corresponding 3D results are illustrated in Fig. S4 and Fig. S5.

6. List of supplementary movies

Movie S1. A bright-field micro-aneurysm-on-a-chip experimental video segment, from which the velocity and pressure fields of blood flow were inferred by the AIV model. The original images were recorded with a frame rate of 500 fps, while the video here has been slowed down to 12.5 fps.

Movie S2. A fluorescence-stained micro-aneurysm-on-a-chip experimental video segment, from which we performed platelet-tracking to obtain the local velocities of the flow. The original images were recorded with a frame rate of 60 fps, while the video here has been slowed down to 12.5 fps.

References

1. X Glorot, Y Bengio, Understanding the difficulty of training deep feedforward neural networks in *Proceedings of the thirteenth international conference on artificial intelligence and statistics*. pp. 249–256 (2010).
2. DP Kingma, J Ba, Adam: A method for stochastic optimization. (30 Jan 2017).
3. X Jin, S Cai, H Li, GE Karniadakis, NSFnets (Navier-Stokes flow nets): Physics-informed neural networks for the incompressible Navier-Stokes equations. *J. Comput. Phys.* **426**, 109951 (2021).
4. S Wang, Y Teng, P Perdikaris, Understanding and mitigating gradient pathologies in physics-informed neural networks. arXiv preprint arXiv:2001.04536 (13 January 2020).
5. B Horn, B Schunck, Determining optical flow. *Artificial Intelligence* **17**, 185–203 (1981).
6. G Aubert, R Deriche, P Kornprobst, Computing optical flow via variational techniques. *SIAM J. on Appl. Math.* **60**, 156–182 (1999).
7. A Bruhn, J Weickert, C Feddern, T Kohlberger, C Schnorr, Variational optical flow computation in real time. *IEEE Transactions on Image Process.* **14**, 608–615 (2005).
8. T Corpetti, D Heitz, G Arroyo, E Mémin, A Santa-Cruz, Fluid experimental flow estimation based on an optical-flow scheme. *Exp. Fluids* **40**, 80–97 (2006).
9. T Liu, L Shen, Fluid flow and optical flow. *J. Fluid Mech.* **614**, 253–291 (2008).
10. D Heitz, E Mémin, C Schnörr, Variational fluid flow measurements from image sequences: synopsis and perspectives. *Exp. Fluids* **48**, 369–393 (2010).

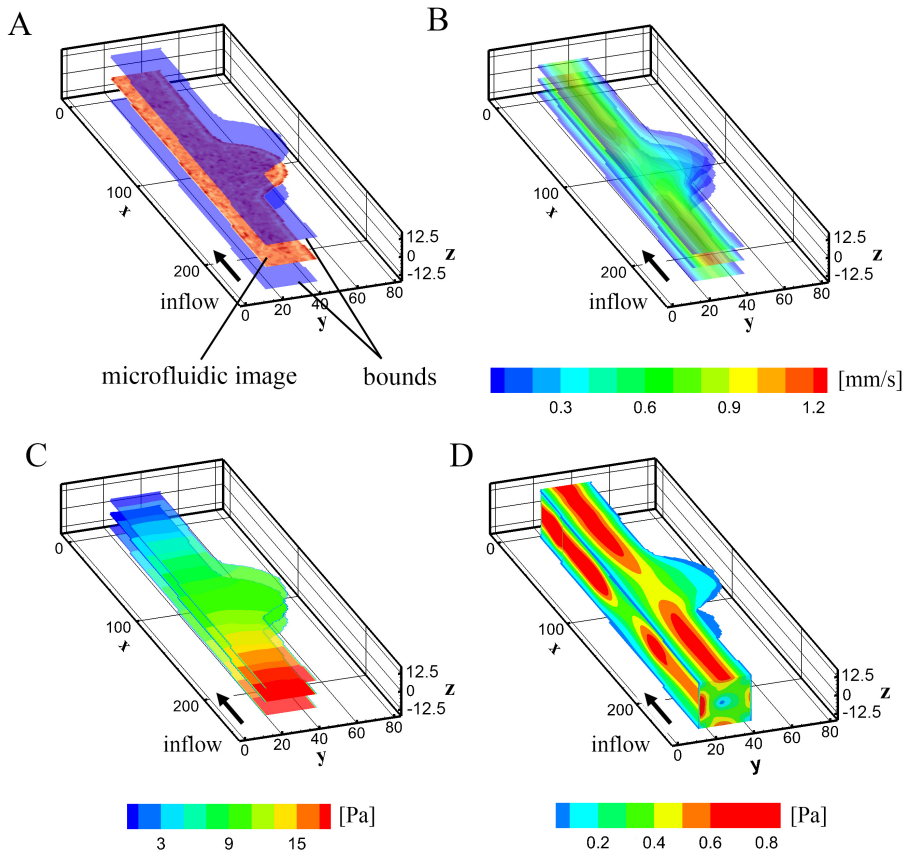

Fig. S4. 3D AIV predictions for MAOAC channel with BNR = 2. (A) A 3D computational domain is constructed by extruding the 2D domain along the depth direction (z) by 25 μm ($z \in [-12.5, 12.5]$ μm), consistent with the depth of the MAOAC channels. We assume that the microfluidic images capture the motion of blood cells at the middle plane in the channel depth direction ($z = 0$). (B) Velocity magnitudes and (C) pressure fields at three different cross-sections ($z = 0, \pm 7.5$ μm) along the depth of the channel. (D) Shear stress on the channel wall. AIV results are averaged over 100 image frames.

11. S Cai, J Liang, Q Gao, C Xu, R Wei, Particle image velocimetry based on a deep learning motion estimator. *IEEE Transactions on Instrumentation Meas.* **69**, 3538–3554 (2020).
12. S Cai, et al., Deep-PIV: a new framework of PIV using deep learning techniques in *13th Int. Symp. on Particle Image Velocimetry, Munich, Germany.* (2019).
13. P Espanol, P Warren, Statistical mechanics of dissipative particle dynamics. *Eur. Lett.* **30**, 191 (1995).
14. RD Groot, PB Warren, Dissipative particle dynamics: Bridging the gap between atomistic and mesoscopic simulation. *The J. Chem. Phys.* **107**, 4423–4435 (1997).
15. DA Fedosov, W Pan, B Caswell, G Gompper, GE Karniadakis, Predicting human blood viscosity in silico. *Proc. Natl. Acad. Sci. U.S.A* **108**, 11772–11777 (2011).
16. T Ye, N Phan-Thien, CT Lim, Particle-based simulations of red blood cells - a review. *J. Biomech.* **49**, 2255–2266 (2016).
17. X Fan, N Phan-Thien, S Chen, X Wu, T Yong Ng, Simulating flow of dna suspension using dissipative particle dynamics. *Phys. Fluids* **18**, 063102 (2006).
18. DA Fedosov, B Caswell, GE Karniadakis, A multiscale red blood cell model with accurate mechanics, rheology, and dynamics. *Biophys. J.* **98**, 2215–2225 (2010).
19. RD Groot, PB Warren, Dissipative particle dynamics: bridging the gap between atomistic and mesoscopic simulation. *J. Chem. Phys.* **107**, 4423–4435 (1997).
20. IV Pivkin, GE Karniadakis, Accurate coarse-grained modeling of red blood cells. *Phys. Rev. Lett.* **101**, 118105 (2008).
21. A Yazdani, GE Karniadakis, Sub-cellular modeling of platelet transport in blood flow through microchannels with constriction. *Soft Matter* **12**, 4339–4351 (2016).
22. H Lei, GE Karniadakis, Probing vasoocclusion phenomena in sickle cell anemia via mesoscopic simulations. *Proc. Natl. Acad. Sci. U.S.A* **110**, 11326–11330 (2013).

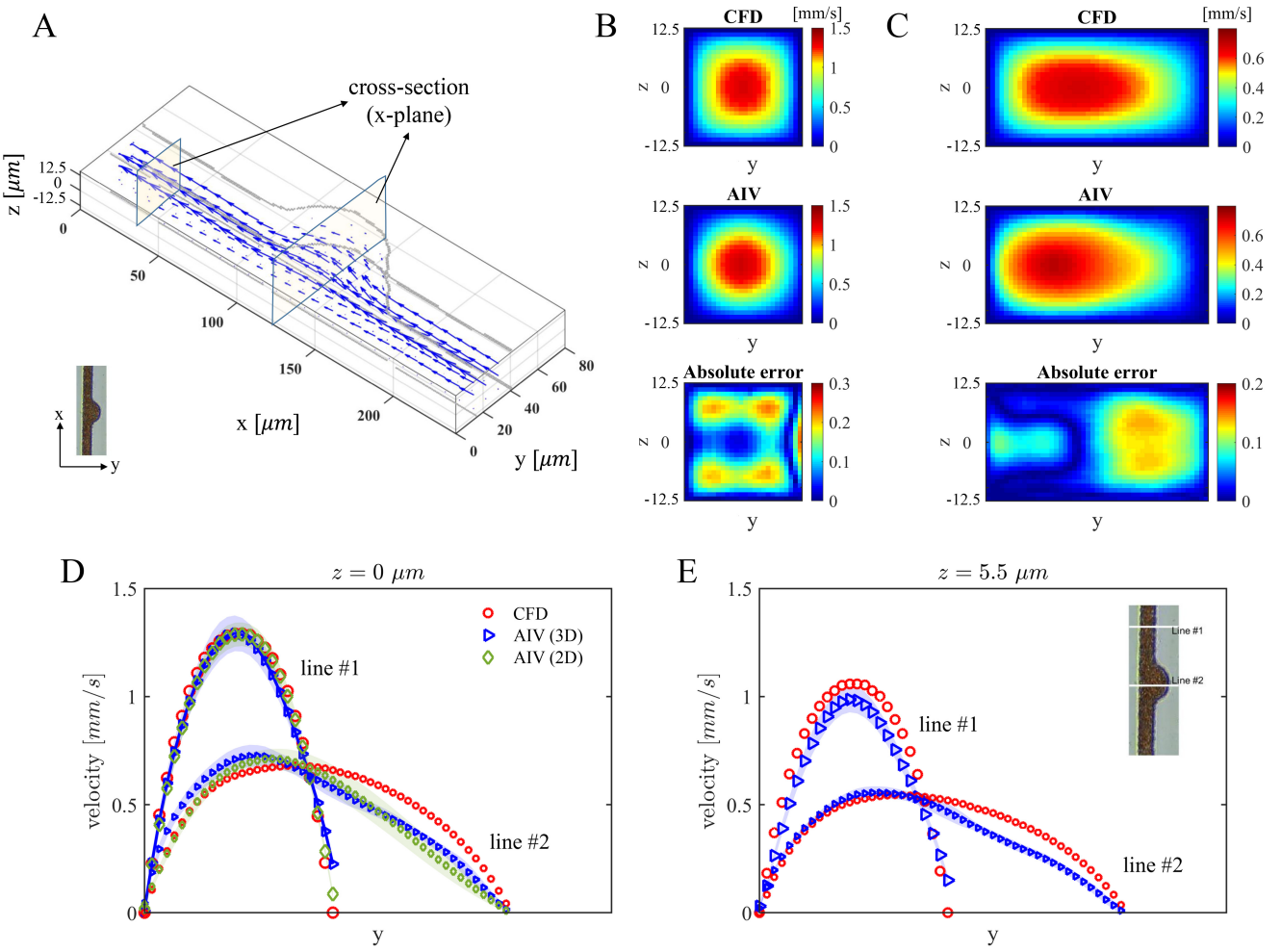

Fig. S5. Comparison of 3D AIV predictions with results of CFD simulations for MAOAC channel with BNR = 2. (A) 3D velocity vectors inferred from AIV. Two cross-sections along the x-axis are selected to make comparisons with CFD simulations. (B) Velocity magnitudes at the cross-section located at $x = 35$ μm in the microchannel. From top to bottom: CFD simulation, AIV model, and absolute error. The relative L_2-norm error at this cross-plane is 14.23%. (C) Velocity magnitudes at the cross-section located at $x = 130$ μm in the microchannel. From top to bottom: CFD simulation, AIV model, and absolute error. The relative L_2-norm error is 16.49%. (D)-(E) Velocity profiles along two cross lines at planes $z = 0$ μm and $z = 5.5$ μm. The symbols of AIV predictions signify the time-averaged values from 100 image frames and the shadows represent the standard deviations.